

# Lawrence Berkeley National Laboratory

## Recent Work

### Title

MICROSTRUCTURE, ADHESION AND GROWTH KINETICS OF PROTECTIVE SCALES ON METALS AND ALLOYS

### Permalink

<https://escholarship.org/uc/item/32m0m75k>

### Authors

Hindam, H.  
Whittle, D.P.

### Publication Date

1982-07-01



# Lawrence Berkeley Laboratory

UNIVERSITY OF CALIFORNIA

## Materials & Molecular Research Division

Submitted to Oxidation of Metals

MICROSTRUCTURE, ADHESION AND GROWTH KINETICS  
OF PROTECTIVE SCALES ON METALS AND ALLOYS

H. Hindam and D.P. Whittle

July 1982

RECEIVED  
LAWRENCE  
BERKELEY LABORATORY  
JUL 16 1982  
LIBRARY AND  
DOCUMENTS SECTION

### TWO-WEEK LOAN COPY

*This is a Library Circulating Copy  
which may be borrowed for two weeks.  
For a personal retention copy, call  
Tech. Info. Division, Ext. 6782.*



LBL-15004  
c.2

## **DISCLAIMER**

This document was prepared as an account of work sponsored by the United States Government. While this document is believed to contain correct information, neither the United States Government nor any agency thereof, nor the Regents of the University of California, nor any of their employees, makes any warranty, express or implied, or assumes any legal responsibility for the accuracy, completeness, or usefulness of any information, apparatus, product, or process disclosed, or represents that its use would not infringe privately owned rights. Reference herein to any specific commercial product, process, or service by its trade name, trademark, manufacturer, or otherwise, does not necessarily constitute or imply its endorsement, recommendation, or favoring by the United States Government or any agency thereof, or the Regents of the University of California. The views and opinions of authors expressed herein do not necessarily state or reflect those of the United States Government or any agency thereof or the Regents of the University of California.

MICROSTRUCTURE, ADHESION AND GROWTH KINETICS  
OF PROTECTIVE SCALES ON METALS AND ALLOYS<sup>x</sup>

H. Hindam<sup>+</sup> and D. P. Whittle<sup>o</sup>

Molecular and Materials Research Division  
Lawrence Berkeley Laboratory

and  
<sup>o</sup>Department of Materials Science and Mineral Engineering  
University of California  
Berkeley, California 94720

ABSTRACT

Current understanding of the complex interrelationships between growth kinetics, microstructure and adhesion of protective  $\text{Cr}_2\text{O}_3$  and  $\text{Al}_2\text{O}_3$  scales are critically reviewed. Similarities and differences in the behavior of these two systems are highlighted. The morphology of the alloy/scale interface appears to be a critical factor. Recent ideas are advanced to interpret the effect of oxygen-active elements on the development of a tortuous interface conducive to improved scale tenacity.

---

<sup>x</sup>This work was supported by the Director, Office of Energy Research, Office of Basic Energy Sciences, Materials Sciences Division of the U. S. Department of Energy under Contract No. DE-AC03-76SF00098.

<sup>+</sup>Present Address: Physical Metallurgy Research Laboratories, CANMET, Ottawa, Ont., K1A0G1; on leave to Industrial Materials Research Institute, NRC, Montreal, Que., H4C 2K3.

## 1. INTRODUCTION

Alloys or metallic coatings, which are designed to withstand high temperature degradation in aggressive environments, rely on the formation of a continuous, adherent, slowly growing oxide scale for corrosion protection. They form scales based principally on either  $\text{Cr}_2\text{O}_3$ ,  $\text{Al}_2\text{O}_3$  or the least investigated,  $\text{SiO}_2$  as major constituents, thus meeting these criteria and ensuring useful lifetimes for alloy components. This requirement then sets certain compositional limits on the alloy active solute content which are necessary for the formation of a continuous protective scale. Nevertheless, such an alloy does not necessarily develop a protective behavior at the onset of the reaction, nor indeed will it maintain it indefinitely since the constitution (morphology and composition) of the scale is time dependent.

Generally, as illustrated in Figure 1, three stages are recognized in the oxidation of an alloy: an incipient, 'transient' stage characterized by the simultaneous formation of the oxides of every active component; a 'steady state' stage coinciding with the development of a protective film and governed by the continued growth of this continuous layer; and finally, and ensuingly accelerated attack or 'breakaway' stage. In terms of practical oxidation behavior, three critical factors can be identified, their relative importance depending on the particular application that the alloy is required to function: (i) the duration of the 'steady state' period, or time to 'breakaway', (ii) the 'pre-breakaway' oxidation rate, which is essentially the growth rate of the protective oxide, and (iii) the 'post-breakaway' oxidation rate. In most applications, factor (i) is most critical; however, it is often very dependent on the growth rate, morphology, composition, etc. of the protective oxide phase, i.e., factor (ii).

Although the objectives of this paper encompass those of separate, relatively recent, reviews on the high temperature oxidation aspects of  $\text{Cr}_2\text{O}_3$  or  $\text{Al}_2\text{O}_3$  forming alloys<sup>(1,3)</sup>, a collective treatment of available as well as recent data and observations, pertinent to protective growth in both systems, seemed necessary to further the understanding of the behavioral mechanisms. After defining the conditions of protective film growth and a brief review of relevant transport properties, typical metallographic observations are presented and interpreted with respect to their relevance and implication on the growth mechanisms. Kinetic data, which were compiled from numerous sources, are effectively analyzed in terms of existing oxidation models. Based on this treatment, fundamental and practical conclusions are deduced in relation to the scale growth mechanisms and alloy behavior in aggressive oxidizing environments. In addition to examining the similarities and differences in the behavior of the two systems, the interdependence of growth kinetics, microstructure and adhesion of the scales are emphasized throughout the text.

## 2. COMPOSITIONAL REQUIREMENTS

Figure 2 is a typical isothermal section (1000°C) in the Ni-Al-O phase diagram<sup>(4)</sup>. Similar data for other Cr and Al containing binary alloys are available: Ni-Cr-O<sup>(5)</sup>, Fe-Cr-O<sup>(6,7)</sup> and Fe-Al-O<sup>(8,9)</sup>. Thermodynamic calculations indicate that  $\text{Al}_2\text{O}_3$ <sup>(10)</sup> and  $\text{Cr}_2\text{O}_3$ <sup>(11)</sup> are stable in contact with alloys containing trace or very small amounts of Al and Cr, respectively.

Although stable over virtually the entire alloy composition range, whether these oxide phases are able to form as continuous layers depends on the relative diffusion rates in the alloy and scale<sup>(12,13)</sup>, and consequently on the alloy bulk composition and oxygen potential in the ambient gas phase. According to these analyses, the minimum solute concentration, necessary for the establishment of a continuous film, is around 13-25 wt.% for  $\text{Cr}_2\text{O}_3$  and 1-8 wt.% for  $\text{Al}_2\text{O}_3$  in oxygen at atmospheric pressure.

In principle, agreement with the experimental observations is satisfactory. However, there are complicating factors, including the effect of additional alloy components and the presence of structural heterogeneities in the alloy. A finer alloy grain size<sup>(14,15)</sup> and the incorporation of oxygen-active elements or their oxides in the form of dispersoids<sup>(2)</sup> promote selective oxidation and the formation of a continuous scale at solute concentrations lower than otherwise predicted. Several models, based on the following concepts, were evoked to rationalize these observations: oxygen gettering by the active elements<sup>(16)</sup> whereby the rapid establishment of a surface oxide film reduces the oxygen activity allowing the outward migration of the solute to form a continuous layer; preferential heterogeneous nucleation of oxide at structural discontinuities which effectively decreases the internuclei spacings<sup>(17)</sup>, and enhanced solute diffusivity in the alloy due to multicomponent interaction effects<sup>(18)</sup>

or short-circuit paths<sup>(19,20)</sup> (e.g. grain boundaries or sub-boundaries, disperse interfaces, etc...). Experimental evidence substantiating or otherwise the last two interpretations were advanced. For instance, in situ SEM observations confirmed preferential nucleation of  $\text{Cr}_2\text{O}_3$  at heterogeneities in Ni 30 Cr\* and Ni 20 Cr 2 v %  $\text{ThO}_2$  alloys<sup>(21)</sup>; tracer diffusion measurements inferred enhanced Cr diffusivity along grain boundaries in a Ni 20 Cr alloy<sup>(22)</sup> and sub-boundaries induced by the fine particles in a thoriated Ni alloy<sup>(23,24)</sup>, but was slightly reduced by small Y addition in elemental form<sup>(25)</sup>; determination of the off-diagonal diffusion coefficients in NiCrAl<sup>(26)</sup> and CoCrAl<sup>(27)</sup> systems did not confirm the presumed role of multicomponent interaction.

Although the factors affecting the development of continuous scale cannot be fully quantitatively analyzed as detailed above, there has been a number of empirical attempts at setting the critical composition limits. These data are conveniently presented in the form of 'oxide maps'<sup>(28,29)</sup>. Figure 3 shows a typical map for the NiCrAl system, displaying the composition ranges over which external scales of  $\text{Al}_2\text{O}_3$ ,  $\text{Cr}_2\text{O}_3$  and NiO predominate. Typical superalloy and coating compositions are superimposed on the diagram. This type of oxide map, although empirical, helps to point the way for alloy development, especially when maps for different temperatures and exposure conditions are compared.

---

\*Alloy compositions are given in weight percentage except when otherwise stated.



### 3. POINT DEFECT STRUCTURES AND TRANSPORT PROPERTIES

$\text{Cr}_2\text{O}_3$  and  $\text{Al}_2\text{O}_3$  are the only thermodynamically stable solid oxides in the Cr-O and Al-O systems, respectively. Corundum ( $\alpha\text{-Al}_2\text{O}_3$ ), stable at temperatures exceeding  $950^\circ\text{C}$ <sup>(30)</sup> and chromia have an identical crystal structure consisting of a hexagonal close-packing of oxygen ions with the trivalent cations occupying 2/3 of the octahedral interstices<sup>(31)</sup>.  $\text{Cr}_2\text{O}_3$  is essentially a semiconductor; whereas  $\text{Al}_2\text{O}_3$  is a mixed conductor with predominant ionic disorder<sup>(32)</sup>. Although the point defect structure of either phase is a matter of conjecture, it is evident that they exhibit a small ( $\text{Cr}_2\text{O}_3$ )<sup>(33)</sup>, or minute ( $\text{Al}_2\text{O}_3^*$ )<sup>(32)</sup>, compositional homogeneity range unamenable to precise determination. Furthermore, the transport properties of these oxide phases are impurity and microstructurally sensitive. The available diffusion data for  $\text{Cr}_2\text{O}_3$ <sup>(34,37)</sup> and  $\text{Al}_2\text{O}_3$ <sup>(38-41)</sup> are compiled in Figure 4.

Oxygen migration in single  $\text{Cr}_2\text{O}_3$  crystals is about 3 orders of magnitude slower than Cr in hot pressed fully dense compacts<sup>(35,36)</sup> suggesting predominant cation disorder. The location of an inert marker subsequent to oxidation of the essentially  $\text{Cr}_2\text{O}_3$  forming Ni 30 Cr alloy supports this conclusion<sup>(42)</sup>. Whereas the actual cation transport mechanism is debatable, Kofstad and Lillerud<sup>(1)</sup> have rationalized the available data in support of an interstitial mode ( $\text{Cr}_i^{2+}$ ). Enhanced diffusivity at reduced oxygen potential<sup>(35)</sup> and the lack of a definitive observation supporting a positive dependence of the oxidation rate constant on the oxygen potential in the form  $k \propto P_{\text{O}_2}^{1/n}$  are in accord with this model<sup>(1)</sup>. As pointed out<sup>(1)</sup>, the observed enhanced sintering rates at reduced  $P_{\text{O}_2}$ <sup>(43-46)</sup> is also consistent with an n-type defect model: oxygen vacancies being the minority defect. Inert marker measurements

---

\* $\text{Al}_2\text{O}_3$  is used throughout the text to designate the corundum phase.

carried out on Ni 20 Cr alloys containing 3 v%  $Y_2O_3$ <sup>(17)</sup> or 2 v%  $ThO_2$ <sup>(29,42)</sup> inferred that the relative diffusivities of Cr and oxygen are influenced by the dispersoids causing a fundamental change in the growth mechanism to predominant oxygen transport as rate controlling.

All tracer diffusion measurements pertaining to  $Al_2O_3$  were carried out at temperatures exceeding the range of interest to alloy oxidation so that extrapolation to lower temperatures is inevitable. Both Al and oxygen are mobile in  $Al_2O_3$  and diffuse at approximately the same rate in polycrystalline specimens. There is considerable disagreement between the data reported for oxygen diffusion in single crystals<sup>(38,40,41)</sup> which was ascribed to differences in purity<sup>(38)</sup>, or non-equilibrium (higher) concentration of defects<sup>(41)</sup> ( $V_O^{\bullet}$  implied) remaining in un-preannealed samples from the low  $P_{O_2}$  environment during crystal growth or sintering. However, it is evident that oxygen transport is significantly enhanced by a smaller grain size<sup>(38)</sup>. It has been proposed that this accelerated boundary transport is associated with interstitial oxygen atoms ( $O_i^x$ )<sup>(47)</sup>. Similarly to  $Cr_2O_3$  scales, inert marker observations indicated that oxygen transport is predominant in an  $Al_2O_3$  scale formed on an active element containing alloy (FeCrAlY)<sup>(48)</sup>. The latter conclusion was recently corroborated based on  $O^{18}$  tracer diffusion measurements in  $Al_2O_3$  scales formed on NiCrAlZr alloys<sup>(49)</sup>. Profuse scale spallation in the case of undoped alloys prevented a definitive conclusion.

For a more detailed discussion of this subject, the reader is referred to the recent reviews on  $Cr_2O_3$  by Kofstad and Lillerud<sup>(1)</sup> and on both oxide phases by Kröger<sup>(32)</sup>.

#### 4. STRUCTURAL FEATURES OF THE SCALES

In this section, typical structural characteristics of the protective scales, selected from the authors' own observations as well as others, are presented under the following headings: (1) oxide ridge development; (2) scale microstructure including grain size, distribution and shape, voids and porosity, and filamentary growth; (3) morphology of the scale/substrate interface embracing the 'rare earth or active element effect'. With minor distinctions, these features are common to both  $\text{Cr}_2\text{O}_3$  and  $\text{Al}_2\text{O}_3$  scales. Their development, influences on the growth rate and their implications on the growth mechanisms and scale adhesion or 'breakaway' are particularly stressed.

##### 4.1 Oxide Ridge Development

Submicron-thick  $\text{Cr}_2\text{O}_3$ <sup>(50)</sup> and  $\text{Al}_2\text{O}_3$ <sup>(51,52)</sup> films are uniform and macroscopically structureless. However, more developed films and scales are non-uniform, exhibiting localized oxide protrusions<sup>(50)</sup> or intrusions<sup>(53)</sup> or a combination of both features<sup>(51-54)</sup>. An illustration is given in Figure 5 for a  $\text{Cr}_2\text{O}_3$  scale formed on pure Cr<sup>(55)</sup> and  $\text{Al}_2\text{O}_3$  film on Ni 32 Al<sup>(52)</sup>. The thick ridges have an ultra-fine grain size in contrast with the adjoining, thinner, well oriented monocrystalline film<sup>(52,56)</sup>. The development of these localized growths is influenced by the orientation of adjacent alloy grains<sup>(52,55,56)</sup>, their surface substructure<sup>(57)</sup> and consequently, by surface preparation techniques<sup>(55-57)</sup>.

It was suggested that this localized scale thickening infers that grain boundaries act as 'easy paths' for the transport of either one reactant ( $\text{Cr}$ <sup>(50)</sup>; O in  $\text{Cr}_2\text{O}_3$ <sup>(55,56)</sup> or  $\text{Al}_2\text{O}_3$ <sup>(51,53)</sup>) or both species ( $\text{Al}_2\text{O}_3$ <sup>(52,54)</sup>). Furthermore, localized scale detachment from substrates with the eventual development of a convoluted morphology and the extensive cracking at tempera-

ture were also attributed to preferential oxygen boundary migration<sup>(55,56,58-62)</sup>. This behavioral aspect is discussed separately in the following section. As reported earlier,  $\text{Cr}_2\text{O}_3$  grows on Cr or its 'pure' alloys by cation transport; nevertheless, oxygen isotope exchange measurements<sup>(63,64)</sup> and a sulfur decoration technique<sup>(65)</sup> inferred anion transport by mechanisms other than lattice diffusion.

Random, outward nodular growths of  $\text{Cr}_2\text{O}_3$  on Ni 20 Cr<sup>(17)</sup>, Co 21 Cr<sup>(66)</sup> and Fe 16 Cr<sup>(67)</sup> alloys, each containing 3 v%  $\text{Y}_2\text{O}_3$ , was associated with the uneven distribution of the dispersoids in the alloys which were prepared by a 'mechanical alloying' technique. This behavior was interpreted by dispersoid - induced hindrance to outward cation diffusion and a reduction in grain size conducive to a fundamental change in the growth mechanism<sup>(17)</sup>, as alluded to in the preceding section.

#### 4.2 Scale Microstructure

Typical fracture sections of a  $\text{Cr}_2\text{O}_3$  and  $\text{Al}_2\text{O}_3$  scales are depicted in Figure 6. Whilst the grain size (submicron) and shape (equi-axed) in  $\text{Cr}_2\text{O}_3$  are usually fairly uniform<sup>(68,69)</sup>, considerable variation is conspicuous across the  $\text{Al}_2\text{O}_3$  scales<sup>(51-53, 70-76)</sup>: the morphology gradually changes from fine equiaxed grains, submicron in size, at the outer interface, to coarse, few microns large, roughly hexagonal columnar grains extending towards the inner interface parallel to the growth direction. This distinct grain size variation, also present in thin films<sup>(77)</sup>, is consistent with inward oxygen diffusion if grain boundaries are assumed as 'short-circuit' paths<sup>(51,73,75)</sup> or alternatively, with outward Al diffusion if the effect of grain growth is taken into consideration<sup>(78)</sup>. Thence, it is evident that this metallographic observation is equivocal with respect to establishing the growth mechanism.

In both instances, the characteristic morphologies are not altered by reactive element additions<sup>(68,79)</sup>, although the actual grain size is significantly reduced<sup>(17,68,79-81)</sup>. The preferential nucleation model, advanced by Stringer et al.<sup>(17)</sup>, which accounts for enhancing selective oxidation, also rationalizes the latter observation in the case of formation of  $\text{Cr}_2\text{O}_3$  on dispersoid containing alloys; albeit grain boundary pinning<sup>(79)</sup> by second phase particles dispersed throughout the  $\text{Al}_2\text{O}_3$  scale<sup>(48,79,82)</sup> should be a significant factor in the case of this relatively more thermodynamically stable phase.

Grain size distribution, as well as grain growth rate<sup>(51,52,77)</sup> and structural development<sup>(3,61)</sup> in  $\text{Al}_2\text{O}_3$  films and scales are well documented. No similar data are available for  $\text{Cr}_2\text{O}_3$  scales, however. A quantitative assessment of the effect of grain boundary transport is deferred until the kinetic data are presented.

Intergranular voids of various shapes and microporosity (10 ~ 200 nm) dispersed within the grains were observed in  $\text{Al}_2\text{O}_3$  films<sup>(77)</sup>. The eventual growth of these voids into large, isolated inner pores indicated that an Ostwald ripening process was operative<sup>(77)</sup>. The distribution of porosity across the film was consistent with a model based on oxygen vacancy supersaturation and precipitation by coalescence<sup>(77)</sup>.

Unlike the oxygen-active element containing alloys, scales formed on the pure alloys exhibit filaments at the outer interface<sup>(48,52,59,68-75)</sup>. Plastic deformation induced by compressive growth stresses, associated with oxygen inward diffusion<sup>(48,74)</sup> or, alternatively, enhanced cation diffusion along a line defect in the whisker core<sup>(83-86)</sup> were suggested as plausible mechanisms for this common observation.

### 4.3 Morphology of the Scale/Substrate Interface

Due to the dramatic effect of active element additions<sup>(2)</sup>, the microstructural details of the scale/substrate interface of the 'pure' and 'doped' alloys are discussed separately.

#### A. *Pure Alloys*

Active element-free alloys exhibit either a relatively planar scale/substrate interface or a convoluted detached morphology. Scales formed on these alloys either crack at temperature or spall profusely upon cooling. Large, oxide free cavities, which may or may not be associated with the convoluted morphology, are consistently observed.

#### 4.3.1 Development of a Convoluted Morphology

Typical micrographs, illustrating the wrinkled configuration, are included in Figure 7. Whereas single layer convoluted scales were usually observed on alloys<sup>(56,62,87,88)</sup>, the formation of multilayers, inferring repeated cracking and healing at temperature, were also observed on pure Cr<sup>(55,56,59)</sup>. In the case of chromium containing alloys, this process is unlikely, except for high Cr contents<sup>(55,58,88)</sup>, since the alloy interdiffusion coefficient<sup>(89,90)</sup> and the diffusivity of Cr in Cr<sub>2</sub>O<sub>3</sub><sup>(34,35,37)</sup> are of such magnitude that selective oxidation results in an appreciable chromium depletion in the alloy region contiguous to the interface<sup>(91-96)</sup>. Upon breakdown, this would normally lead to the formation of stratified scales<sup>(68,97-99)</sup> consisting of the faster growing oxide of the more noble metals. In contrast, since diffusion in Al<sub>2</sub>O<sub>3</sub> scales<sup>(38-41)</sup> is much slower than in the alloy<sup>(100)</sup>, no significant Al depletion is anticipated, and indeed was ever detected. Consequently, the formation of multilayers is possible, but seldom observed. This might be due to the ability of the relative thin, slow growing, Al<sub>2</sub>O<sub>3</sub> scales to deform more excessively without fracture than the thick Cr<sub>2</sub>O<sub>3</sub> scales.

However, recent evidence indicates that plastic deformation of the latter is enhanced at reduced  $P_{O_2}$  (59,69). The intensive wrinkling of the  $Al_2O_3$  scale, depicted in Figure 7(b) was observed on FeAl alloys containing Cu (79).

The original model, proposed by Rhines and Wolf (101) to explain the generation of growth stresses in the outwardly growing NiO scale, was adopted by Caplan et al. (55,56) and Wood et al. (3, 60-62) to interpret the development of convoluted configurations in  $Cr_2O_3$  and  $Al_2O_3$  scales, respectively. It is based on preferential oxygen migration along grain boundaries to react with the outward flux of cations at these locations and the consequent formation of 'oxide within existing oxide'. Eventually, the development of large compressive stresses leads to localized detachment and buckling of the scale as reaction proceeds. However, unless an interstitial mechanism is involved, it is difficult to envisage any volume expansion within the oxide layer: fresh lattice sites are only created at the scale interfaces.

An alternative view was proposed by Giggins and Pettit (70) who attributed the phenomenon to the growth and impingement of large  $Al_2O_3$  crystals at the underside of the scale where localized detachment from the alloy substrate has occurred. These crystals form only at these locations, by aluminum evaporation from the substrate, and their unrestrained growth causes scale buckling. However, as discussed later, metallographic evidence fails to support this model.

#### 4.3.2 Cavity Formation

The formation of interfacial cavities of various sizes (1-50  $\mu m$ ) and shapes was first observed by Howes (102,103) and substantiated later by several other investigators (48,51,52,60-62,70-78,104). Figure 8 depicts the alloy/scale interfacial morphology for an Fe 25 Cr and  $\beta$  NiAl (52) which was revealed due to scale spallation upon cooling to room temperature. The exposed alloy

surface shows a number of oxide-free, slightly concave, craters having a smooth, occasionally thermally etched, appearance and representing areas where the scale and substrate were not in intimate contact at reaction temperature. Elsewhere, it exhibits oxide grain 'imprints', where the scale had maintained alloy contact. It is evident that the fractional void area can be significant.

A favored mechanism for cavity formation is vacancy coalescence in the absence of effective sinks. The vacancies are generated, in excess of the saturation limit, by the outward cation diffusion in a p-type scale<sup>(102,105)</sup> (e.g. transient oxides such as FeO, CoO, NiO, etc.) or simply by the incorporation of metal atoms/ions from the substrate into the scale, if the latter does not relax completely to maintain intimate contact with the receding substrate<sup>(106,107)</sup>. Another possible vacancy source, which was attributed by Douglass et al.<sup>(71,72)</sup> as a cause for void formation in scales growing on alloys by predominant inward oxygen transport, is the Kirkendall effect arising from a faster backward diffusion of the noble metal to the alloy bulk than the forward diffusion of the oxidizable metal to the alloy/scale interface. Diffusion measurements in the Ni-Al system<sup>(100)</sup> tend to support this model, although over a restricted range of alloy composition, specifically the Ni-rich side of the  $\beta$ -NiAl phase field.

The second major view of void or cavity development centers around the development of lateral compressive growth stresses in the scale, particularly if there is oxide formation within the scale itself<sup>(3, 60-62)</sup>, as discussed earlier. The tendency towards the formation of a convoluted morphology results in localized loss of scale adhesion and cavity formation at the interface, especially at structural discontinuities. This effect is intensified by the relatively high vaporization rate of the active metal from the substrate<sup>(48,51, 52,70,102)</sup> which is evident in the accompanying micrographs (Figure 8).



Inspection of Figures 5(b), 7(b) and 9(a) indicate that neither the scale grain morphology nor its growth rate are affected by cavity formation or local detachment and the development of a convoluted configuration. The former observation does not substantiate the grain growth and impingement model<sup>(70)</sup>, alluded to earlier, to interpret scale convoluted growth. In support to the latter part of the previous conclusion, it was demonstrated that the aluminum evaporation rate from the substrate, at the reaction temperature, is sufficient to sustain the observed growth rate of  $Al_2O_3$  scales<sup>(52,70)</sup>.

The poor scale adhesion was attributed to lateral scale growth<sup>(3,55,56, 60-62)</sup> under the influence of stresses generated by the mechanism<sup>(101)</sup> discussed above or to concentration of athermal stresses around the cavities<sup>(48,70-72)</sup>.

#### B. Active-Element Containing Alloys

Scales formed on alloys containing active elements are tenacious or at least adherent to their substrates<sup>(2)</sup>. In contrast to the pure alloys, they exhibit a tortuous interface due to the development of inwardly growing pegs\*. A typical illustration is given in Figure 9(b) for an  $Al_2O_3$  scale formed on Fe10Al1Hf alloy<sup>(82)</sup>. The growth of this type of peg is closely related to the distribution of the  $HfO_2$  dispersoids in the scale. The presence of these embedded particles as well as unreacted Fe inclusions in the scale offer additional support to the inward growth model for  $Al_2O_3$  scales on these alloys.

#### 4.3.3 Peg Growth Mechanism

The present authors have interpreted<sup>(82)</sup> the development of such circuitous interface in FeAlHf<sup>(82)</sup> and a similar morphology in FeCrAlSc<sup>(48)</sup>

---

\*Typical metallographic observations can be found in references: 20, 48, 53, 60-62, 70, 73-76, 79, 82, 104, 108-112.

alloys by a short-circuit diffusion model involving localized enhanced oxygen transport in the oxide particles of the active element present in the scale. In addition to metallographic observations, oxygen diffusion data<sup>(113)</sup> are confirmatory evidences for this model since diffusion in the highly oxygen-deficient oxides of the active elements is several orders of magnitude faster than in the host  $\text{Al}_2\text{O}_3$  scale.

#### 4.3.4 Adhesion Mechanism

The suppression of scale detachment, its convoluted growth and the remarkable improvement in its tenacity to substrates, which are induced by active element addition, are the subject of several controversial interpretations.

Wood et al.<sup>(3, 60-62)</sup> attributed the phenomenon to a change in the growth mechanism which is in essence similar to the model, discussed earlier, advanced by Stringer et al.<sup>(17,66)</sup> to explain the improved adhesion and anomalous growth behavior of  $\text{Cr}_2\text{O}_3$  scales on dispersed oxide containing alloys. They suggested that the incorporation of Y into the  $\text{Al}_2\text{O}_3$  scale suppresses the cation contribution to scale growth, thus shifting the reaction from the scale interior to its inner interface. It is implicitly assumed that this would result in a significant reduction in growth stresses. In their recent review<sup>(3)</sup>, they claim this is consistent with the views, and work, of Kroger<sup>(32,114)</sup> who suggests that Y acts as a donor, presumably because of its large ionic radius. This donor activity compensates the iron acceptors in  $\text{Al}_2\text{O}_3$ : Fe, and thus, by reducing the concentration of interstitial Al ions without markedly increasing that of Al vacancies, explains how Al transport outward is stifled. Alternatively, since the active elements inhibit cavity formation, the improvement in adhesion was attributed<sup>(17,22,25,48,70-72,80,81,76,115-118)</sup> to these additions (either in elemental or dispersed oxide forms) acting as

efficient vacancy sinks, as originally proposed by Stringer<sup>(119)</sup>.

Whilst the foregoing mechanism might be operative at the incipient reaction stage, when the vacancy flux is at its maximum, a body of detailed metallographic evidences and the application of a microindentation technique by the present authors<sup>(79,82)</sup> confirmed that 'pegging' or 'mechanical keying' is the most pertinent factor in the adhesion of 'mature scales', as originally suggested by Lustman<sup>(108)</sup>. Within this context, a sample preparation technique<sup>(120,121)</sup>, based on selective chemical dissolution of the alloy substrate, was extremely useful in revealing peg microstructural details which otherwise would not be discernible. Figure 9(b), referred to earlier, is a typical example of a deeply-etched cross section. A systematic interpretation of the active element-induced peg growth mechanisms and morphologies, and their implications on the adhesion of protective scales are the objectives of a future comprehensive publication<sup>(122)</sup>.

Although the subject of convoluted scale morphology and cavity formation is controversial with regard to whether they are the cause or results of poor adhesion, it is evident that enormous stresses are generated by scale growth and are significantly reduced by active element additions. A thorough understanding of how the stress distribution is influenced by the morphology of the interface in 'pure' and active element containing alloys, as well as the mechanical properties of films and scales, including the effect of doping, are prime requisites to elucidate the adhesion mechanism.

## 5. GROWTH KINETICS

As pointed out in the introduction, oxidation of alloys involve three well defined stages. The kinetic data, reported herein and which were compiled from several investigations\*, reflect the 'steady state' stage governed by the growth of protective  $\text{Cr}_2\text{O}_3$  or  $\text{Al}_2\text{O}_3$  scales, as explicitly stated by the original authors.

### 5.1 Pure Chromium

Although pure chromium is not technologically important as an oxidation-resistant structural material, several investigators have studied this presumably simple system to acquire a fundamental insight to the corrosion mechanism. With justifiable reservations, the oxidation kinetics are diffusion controlled at least at some stage of the reaction. Reported values of the parabolic rate constants are compiled in an Arrhenius plot, Figure 10, and the source of these data as well as appropriate annotations are listed in Table I. With the exception of one investigation<sup>(69)</sup>, which was carried in  $\text{CO}/\text{CO}_2$  mixtures of variable compositions, all others were performed in pure oxygen. The lowest data points are based on thickness measurements at locations where the oxide was apparently monocrystalline<sup>(56)</sup>.

The most striking conclusion is that the growth of  $\text{Cr}_2\text{O}_3$ , even on pure Cr, is far from simple. Rate constants at  $1000^\circ\text{C}$  for example, can differ by four orders of magnitude, which means that the observed scale thickness formed after a given exposure can vary by a factor as much as 100. Several variables may have contributed to the inconsistency of the various determinations, namely: purity of the starting metal and impurity doping of  $\text{Cr}_2\text{O}_3$ ; formation of volatile

---

\*A complete reference list is given in Table I through Table IV.

oxide species and finally, differences in oxidation behavior arising from sample preparation and exposure techniques. As the effect of the last two factors on the oxidation kinetics was emphasized, they are discussed below.

Whereas the oxidative vaporization of  $\text{Cr}_2\text{O}_3$  at reduced  $P_{\text{O}_2}$  ( $\text{CO}/\text{CO}_2$  mixtures) is negligible<sup>(69)</sup>, it becomes significant in oxygen-rich atmospheres at  $\sim 1000^\circ\text{C}$ <sup>(124,128-130)</sup>. At temperatures exceeding  $1200^\circ\text{C}$ , a net weight loss is often observed during the course of the reaction. The vaporization rate is enhanced by the speed of the gas stream<sup>(131-133)</sup> and the presence of atomic oxygen<sup>(134)</sup> or water vapor<sup>(135,136)</sup>. Various volatile species, with a general formula  $\text{CrO}_x(\text{OH})_y$  were detected under variable oxidizing conditions. Several authors have corrected their kinetic data based on Hagel's vaporization measurements<sup>(125)</sup>, although not necessarily using a similar experimental set-up or identical conditions. Others attempted to suppress volatilization by surrounding the sample with  $\text{Cr}_2\text{O}_3$  powder to saturate the ambient gas with the volatile species. In few cases, this complication was ignored entirely\*.

The effect of various surface preparation techniques (mechanical abrasion, electropolishing, etching, etc...) and, related to this, the experimental procedure used in initiating the reaction (hot, bare insertion of the sample, heating in vacuum prior to admitting the oxidant, etc...) have received considerable attention\*\*. Presumably, specimen pre-treatment, such as hot rolling, annealing or mechanically working the surface are equally important. Although remarkable differences in oxidation behavior were attributed to a strong dependence of scale morphology (grain size, orientation, etc.) on surface treatment<sup>(55,56)</sup>, no direct correlation was established. Generally, fine grained scales grew considerably faster than those composed of few, large,

---

\*Appropriate annotations are included in Tables I through III to indicate whether volatilization was considered.

\*\*Refer to Figure 1 and Table I for comparison of variation of reaction rate with surface treatment.

well oriented crystallites.

As a consequence of the last factor, and an additional complicating one, which was discussed in the preceding section, is the often observed non-uniform scale growth (nodules, blisters, convolutions, etc.) which obviously can contribute very significantly to weight change measurements. Again, there is little correlation with experimental variables, although the grain shape, size and distribution are clearly involved.

## 5.2 Cr<sub>2</sub>O<sub>3</sub> - Forming Alloys

Apparent parabolic rate constants for the oxidation of binary Fe-, CO- and Ni-Cr alloys in air or pure oxygen are summarized in Figure 11 and a reference list and other pertinent data are given in Table II. Since these measurements are based on weight change, the contribution from transient oxides which are often detected in the scale, is inevitable. In addition, internal precipitation in Cr-rich alloys might occur, although its contribution is less significant. Cr<sub>2</sub>O<sub>3</sub> scales formed on alloys contain limited dissolved amounts of the noble metal which might modify its point defect concentration and consequently its transport properties. Whereas both Ni and CO have small, but significant solubilities in Cr<sub>2</sub>O<sub>3</sub>, Fe<sub>2</sub>O<sub>3</sub> and Cr<sub>2</sub>O<sub>3</sub> are completely isomorphous. The actual amount which would dissolve in the scale depends on the alloy/scale interfacial concentrations which are in turn determined by the interplay between the diffusion rates in the respective phases, as referred to earlier.

Comparison of Figures 10 and 11 indicates that Cr<sub>2</sub>O<sub>3</sub> on alloys, can grow neither as fast, nor as slow as that on pure Cr. However, the measured parabolic rate constants show somewhat less scatter; the variation is only by a factor of 10<sup>2</sup>, making the scale thickness variation after corresponding exposure times only 10 times. Although not apparent in Figure 11, the rate constant tends to increase with Cr content in a given system<sup>(127)</sup>; in addition, NiCr alloys show

less scatter than Fe or Co-Cr alloys.

Kinetic data for active element containing alloys are superimposed on the scatter band for the 'pure alloys' in Figure 12. Refer also to Table III for compositional and other relevant information. Generally, alloys with active additions oxidize at a slower rate. It should be noted that  $\text{Cr}_2\text{O}_3$  scales can grow on the active element containing alloys at a rate as slow as single  $\text{Cr}_2\text{O}_3$  crystallites on Cr. Although the curtailment of the transient oxidation period and the marked amelioration of scale adhesion<sup>(2)</sup>, conferred by the active elements, would contribute to an overall reduction in the thermogravimetrically determined reaction rates, metallographic evidences ascertained that growth of the  $\text{Cr}_2\text{O}_3$  scale is actually hindered<sup>(17,42)</sup>, as discussed in the preceding section.

### 5.3 $\text{Al}_2\text{O}_3$ -Forming Alloys

After a brief period of rapid oxidation, the reaction kinetics of essentially  $\text{Al}_2\text{O}_3$  scale forming alloys, including those containing reactive elements, were characterized by approximate parabolic laws over a relatively short incipient stage (50 ~ 100 hr) and subsequent monotonical decline from this ideal behavior over extended periods\*. Consequently, the 'apparent' parabolic rate constants, which are included in Figure 13, were evaluated based on weight change or scale thickness data at maximum exposure time using appropriate conversion factors. As with the  $\text{Cr}_2\text{O}_3$ -forming alloys, thermogravimetric measurements would include some, however more significant, effects from the transient oxides. However, smaller amounts of the noble metals are dissolved in the scale. Unlike the  $\text{Cr}_2\text{O}_3$  systems and despite these reservations and the wide range of alloy compositions which are included, Table IV, the scatter in the

---

\*Refer to Table IV for specific observations.

data is only about 1.5 orders of magnitude; corresponding to a variation in scale thickness by a factor of 4. No direct correlation between alloy composition or system and growth constant is evident. Furthermore, and in contrast to the  $\text{Cr}_2\text{O}_3$ -forming alloys, the addition of active elements, although causing localized preferential thickening, as was demonstrated metallographically in the preceding section, has no significant influence on the overall oxidation rate.

Variation within the scatter band, are presumably related to subtle variations in the grain size (and morphology) of the  $\text{Al}_2\text{O}_3$  scale, and the possible incorporation of dopants (Fe, Ni, Co, or Cr, or active elements Y, Hf, Ce, Th, etc.) modifying the defect structure and transport properties. However, it should be pointed out that these variables are probably of little practical significance. An  $\text{Al}_2\text{O}_3$  scale growing at the rate indicated at the upper limit of the scatter band would only be 20  $\mu\text{m}$  thick after 1000 h at 1100°C. As a consequence, in terms of oxide thickness, or consumption of Al from the alloy, this is not important. If, however, a faster growth rate implies an earlier onset of breakaway (i.e., loss of protection) then it is rather critical.

Although the diffusivity of the more mobile species in  $\text{Cr}_2\text{O}_3$  and  $\text{Al}_2\text{O}_3$  vary by more than four orders of magnitude, Figure 4, the minimum observed growth rate for both scales unexpectedly coincide, Figures 10 and 13.

#### 5.4 Interpretation

In this subsection, the kinetic data for protective scale growth, documented in Figures 10 through 13, are rationalized by comparing the observed values with those calculated from independent diffusion measurements of the transport rate of the predominantly mobile species in the respective oxide.

##### 5.4.1 $\text{Cr}_2\text{O}_3$ Scales

According to the parabolic oxidation theory<sup>(156,157)</sup>, the rational



growth rate constant for scales with predominant cation (Cr) transport can be defined as:

$$Kr(g \text{ eq/cm. sec}) = \frac{3}{2} \bar{C}_{eq} \int_{a_0^i}^{a_0^x} D_{Cr} d \ln a_0 \quad [1]$$

where  $\bar{C}_{eq} = \frac{\rho_{Cr_2O_3}}{\text{Eqv. Weight}_{Cr_2O_3}}$ , i.e. the average g eqv. of either Cr or O or  $Cr_2O_3$  in the oxide phase per  $cm^3$ ;  $a_0^x$  and  $a_0^i$  are the oxygen activity in the ambient gas and at the scale/metal interface, respectively.

Two defect models are considered:

a. Vacancy Mechanism ( $V_{Cr}^{\alpha'}$ ):

Defect Equation:

$$\frac{3}{2} O_2 = 3 O_0^x + V_{Cr}^{\alpha'} + \alpha h \cdot \quad [2]$$

The corresponding dependence of  $D_{Cr}$  on  $P_{O_2}$  can be expressed as:

$$D_{Cr} \propto P_{O_2}^{1/n} \quad [3]$$

$$\text{where } 1/n = \frac{3}{2(1+\alpha)}$$

b. Interstitial Mechanism ( $Cr_i^{\alpha\cdot}$ ):

The relevant expressions are

$$\frac{3}{2} O_0^x + Cr_{Cr}^x = Cr_i^{\alpha\cdot} + \alpha e' + \frac{3}{4} O_2 \quad [4]$$

$$D_{Cr} \propto P_{O_2}^{-1/n} \quad [5]$$

Substituting equations [3] or [5] in [1] and integrating, noting that

$$a_0 = \sqrt{P_{O_2}}; \rho_{Cr_2O_3} = 5.21 \text{ g/cm}^3;$$

$$Kp(g^2/cm^4 \text{ sec.}) = Kr(g \text{ eq/cm sec.}) \times 8(g \text{ O/g eq}) \times (\rho(g \text{ Cr}_2O_3/cm^3) \times \frac{48}{152} (g \text{ O/g Cr}_2O_3)),$$

the dependence of  $Kp$  on  $P_{O_2}$  are derived as:

$$\text{Vacancy Model: } Kr = \frac{3}{4} n \bar{C}_{eq} D_{Cr}^i \left[ \left( \frac{P_{O_2}^x}{P_{O_2}^i} \right)^{1/n} - 1 \right] \quad [6]$$

$$\text{Interstitial Model: } K_r = \frac{3}{4} n \bar{C}_{eq} D_{Cr}^i \left[ 1 - \left( \frac{P_{O_2}^x}{P_{O_2}^i} \right)^{-1/n} \right] \quad [7]$$

At 1000°C,  $P_{O_2}^i \text{ Cr/Cr}_2\text{O}_3 = 10^{-22} \text{ atm}^{(158)}$ . Assuming  $\alpha = 3$ ; then  $1/n = \frac{3}{16}$  and the coefficient of either expression for  $K_g$  is 10.827. It should be noted that if  $P_{O_2}^x \gg P_{O_2}^i$ , the last expressions are reduced to

$$K_p \simeq 10.827 D_{Cr}^i \left( \frac{P_{O_2}^x}{P_{O_2}^i} \right)^{1/n} \text{ and } 10.827 D_{Cr}^i, \text{ respectively. } D_{Cr}^i \text{ is taken as}$$

$= 0.137 \exp (-61,100/RT)$  based on Hagel's measurements<sup>(35)</sup> and Kofstad and Lillerud's interpretation of these data<sup>(1)</sup>. The relationships [6] and [7] are plotted in Figure 14 as  $K_p$  versus  $P_{O_2}^x$  along with the recent measurements for the parabolic growth of  $\text{Cr}_2\text{O}_3$  on pure Cr at reduced oxygen potentials<sup>(69)</sup>. It should be noted that although for the interstitial model,  $D_{Cr}$  increases as  $P_{O_2}$  is reduced, equation [5],  $K_p$  remains virtually unaffected. Neglecting for the moment the values of the experimental determinations relative to the calculated ones, it is evident that the observed trend, specifically virtual independence on  $P_{O_2}$ , does substantiate the interstitial transport mechanism and offer strong support for the recent suggestions by Kofstad and Lillerud<sup>(1)</sup>. An additional corroboration is that under similar conditions, alloys with sufficient Cr to form a continuous  $\text{Cr}_2\text{O}_3$  scale oxidize at a slower rate than pure Cr which is consistent with the proposed mechanism<sup>(69)</sup>.

Since the growth mechanism has been established, it is now possible to compare the experimental data with derivations based on the proposed defect model and independent diffusion measurements, equation [7]. This was carried out in Figure 15, where the ranges of values of the growth constants on alloys both with and without additions (Figures 10-12) have been combined. For clarity, the individual experimental points have been

omitted. It is evident that the parabolic rate constants derived from the diffusion measurements correspond to the upper limit of the experimental data. Although the scales grown on pure Cr or its alloys exhibited a much finer grain size than the sintered compacts of the diffusion studies, boundary transport would presumably not be as significant as for p-type cation-defective oxides. Based on this analysis which involves only a single, pertinent diffusion study<sup>(35)</sup>, it would be premature to state definitively which data actually represent the diffusion-controlled growth of protective  $\text{Cr}_2\text{O}_3$  scales. However, it is abundantly clear that in addition to diffusion data under well controlled atmospheres, a precise empirical assessment of the effect of volatilization as well as detailed microstructural and compositional characterization of the scales and sintered compacts are essential to resolve the discrepancies between the diffusion and oxidation kinetic data.

#### 5.4.2 $\text{Al}_2\text{O}_3$ Scales

It is not possible to make a comparison between measured and calculated parabolic rate constants, as was attempted for  $\text{Cr}_2\text{O}_3$ , since the pressure dependency of transport in  $\text{Al}_2\text{O}_3$  is not known. Nevertheless, following Smialek<sup>(77)</sup>, the scale may be envisaged as a moving boundary of fixed composition, and thus, its boundaries follow a parabolic law and

$$x^2 \sim D_{\text{eff}} t \sim K_x t \quad [8]$$

where  $x$  is the scale thickness,  $D_{\text{eff}}$  an "effective" diffusion coefficients, and  $K_x$  the parabolic growth constant in terms of scale thickness. This latter parameter is obtained from the gravimetric constant using the density of  $\text{Al}_2\text{O}_3$  ( $3.98 \text{ g/cm}^3$ ) and the ratio of weight of oxygen in  $\text{Al}_2\text{O}_3$  to weight of  $\text{Al}_2\text{O}_3$  ( $\frac{3/2 M_{\text{O}_2}}{M_{\text{Al}_2\text{O}_3}} = 0.235$ ). The  $K_x$ 's or  $D_{\text{eff}}$ 's from Figure 13 are

plotted as a band in Figure 16.

Since no data are available to determine whether Al diffusion is structurally sensitive, the high temperature results for polycrystalline samples (Figure 4) are extrapolated assuming no change in the activation energy and they are included in Figure 16. Extrapolation of single crystal data (characteristic of intrinsic as well as extrinsic lattice diffusion) are shown as a band. Oxygen grain boundary diffusion is assessed by comparing data obtained from polycrystalline and single crystal materials<sup>(77)</sup>. An effective diffusion coefficient,  $D_{eff}$ , is defined, when if grain boundaries represent the major short circuit diffusion path, then

$$D_{eff} \approx (1-F) D_L + F D_{gb} \quad [9]$$

where  $D_L$  and  $D_{gb}$  are the lattice and grain boundary diffusion coefficients respectively, and  $F$  is the effective volume fraction of grain boundaries. For an array of square grains, it can be shown that,

$$F = 2\delta/GS \quad [10]$$

where  $\delta$  is the grain boundary width and  $GS$  is the grain size. Furthermore, if  $D_{gb} \gg D_L$  and  $F \gtrsim 0.1$ , then

$$D_{eff} \approx \frac{2\delta D_{gb}}{GS} \quad [11]$$

The vertically hatched band marked oxygen grain boundary in Figure 16 correspond to  $D_{eff}$  calculated, and extrapolated, from a combination of the measured diffusivities in poly- and single-crystalline  $Al_2O_3$ , using the lower branch of the single crystal data. A value of  $\delta$  of  $100 \text{ \AA}$  (seems to be generally accepted) and a grain size of  $0.1 \text{ \mu m}$  has been used. The spread of values corresponds to the experimental spread in the two sets of original data<sup>(38,40,41)</sup>. Extrapolated values of actual direct measurements<sup>(159)</sup> or grain boundary oxygen diffusion in  $Al_2O_3$  fall within this band.

Finally, the fourth band on Figure 16, diagonally hatched area, correspond

to  $D_{\text{eff}}$  calculated in the same manner as above, but using extrapolated data from the higher branch of the single crystal data (note that this also corresponds to a lower apparent activation energy), for which it will be recalled that it was suggested<sup>(41)</sup> that the higher diffusivities were due to a higher than equilibrium concentration of defects ( $V_{\text{O}}^{\bullet\bullet}$ ) remaining in the sample from the low  $P_{\text{O}_2}$  environment encountered during crystal growth or sintering. The samples were not annealed prior to the diffusion studies; however, the original authors attributed the higher diffusivities to unintentional doping (impurities) of the  $\text{Al}_2\text{O}_3$  powder. The band of data come from using grain sizes in the range 0.1-5  $\mu\text{m}$ ; a constant grain boundary width of 100  $\text{\AA}$  was used.

It is fairly evident then from Figure 16, that the effective diffusivities from scale growth measurements can only correspond to a short circuit diffusion process (0.1-5  $\mu\text{m}$  is a typical range of grain size for  $\text{Al}_2\text{O}_3$  scales), and even then, only to the somewhat untypical results, supposedly characteristic of a high vacancy content. Smialek<sup>(77)</sup> suggests that the  $\text{Al}_2\text{O}_3$  which grows on alloys also contains excess (cf. equilibrium) vacancies, as evidenced by the formation of pores within the growing scale. Elegant transmission micrographs support this view, with more pores forming at the oxide/gas interface where the flux of vacancies, due to the continually growing scale is greatest.

It appears reasonably conclusive, then, that some type of short circuit diffusion process, via grain boundaries, is responsible for the observed growth rates being higher than independent diffusion measurements would suggest. Equally it would seem that oxygen is the more mobile species, at least in fine-grained  $\text{Al}_2\text{O}_3$  scales; but it must be remembered, that the foregoing conclusion is based on a single determination of Al diffusivity at very high temperatures (1670-1905°C)<sup>(39)</sup>. Thus, it seems perfectly reasonable that the extrapolated line in Figure 9 for Al diffusion is too low, and that both Al and O diffusion may contribute to scale growth.

#### CONCLUDING REMARKS

The close interaction between growth kinetics, scale microstructure and adhesion has been demonstrated. This is probably not of major importance in terms of the growth rate of the protective oxide, especially in the case of  $\text{Al}_2\text{O}_3$ , since even growth at the fastest observed rate, does not correspond to a major loss in material in many instances. The spread of growth rates observed for  $\text{Cr}_2\text{O}_3$  scales, however, does encompass unacceptably high rates. Breakdown of the protective scale, especially by mechanical spallation, is critically dependent on the details of the microstructure, and the ability of active element or oxide dispersion additions to modify this is of clear technological importance. This paper has defined the mechanism involved, which is essential to achieve the maximum benefits of these effects.

# REFERENCES

1. P. Kofstad and K. P. Lillerud, J. Electrochem. Soc., 127, 2410 (1980).
2. D. P. Whittle and J. Stringer, Phil. Trans. R. Soc. Lond. A, 295, 309 (1980).
3. G. C. Wood and F. H. Stott, Proc. of NACE Conf. on 'High Temperature Corrosion,' San Diego, California, March (1981).
4. F. Elrefaie and W. W. Smeltzer, J. Electrochem. Soc., 128, 2237 (1981).
5. H. Davies and W. W. Smeltzer, *ibid.*, 121, 543 (1971).
6. A. U. Seybolt, *ibid.*, 107, 147 (1960).
7. M. A. J. Th. Laheij, F. J. J. Van Loo and R. Metselaar, Oxid. Met., 14, 207 (1980).
8. L. M. Atlas and W. K. Sumida, J. Amer. Ceram. Soc., 41, 157 (1958).
9. J. A. Imlach and F. F. Glasser, Trans. J. Br. Ceram. Soc., 70, 227 (1971).
10. F. S. Pettit, Trans. Met. Soc. AIME, 239, 1296 (1967).
11. N. Birks and H. Rickert, J. Inst. Met., 91, 308 (1963).
12. C. Wagner, J. Electrochem. Soc., 99, 369 (1952).
13. D. P. Whittle, G. C. Wood, D. J. Evans and D. B. Scully, Acta Met., 15, 1747 (1965).
14. C. S. Giggins and F. S. Pettit, Trans. Met. Soc. AIME, 245, 2509 (1969).
15. P. Moulin, F. Armanet, G. Beranger and P. Lacombe, Mém. Sci. Rev. Mét., 74, 143 (1977).
16. C. Wagner, Corros. Sci., 5, 751 (1965).
17. J. Stringer, B. A. Wilcox and R. I. Jaffee, Oxid. Met., 5, 11 (1972).
18. J. Stringer, Electric Power Research Institute, Palo Alto, California, Private Communication.
19. C. S. Giggins and F. S. Pettit, Trans. Met. Soc. AIME, 245, 2495 (1969).
20. I. A. Kvernes, Oxid. Met., 6, 45 (1973).
21. H. M. Flower and B. A. Wilcox, Corros. Sci., 17, 253 (1977).
22. P. Moulin, A. M. Huntz, G. Beranger and P. Lacombe, Scrip. Met., 11, 533 (1977).
23. M. J. Fleetwood, J. Inst. Met., 94, 218 (1966).
24. J. D. Whittenberger, Met. Trans., 4, 715 (1973).

25. D. Delaunay, A. M. Huntz and P. Lacombe, *Scrip. Met.*, 13, 419 (1979).
26. A. Green, M. Eng. Thesis, University of Liverpool, United Kingdom (1975).
27. G. W. Roper and D. P. Whittle, *Met. Sci. J.*, 14 (1980).
28. E. Scheil and E. H. Schulz, *Arch. Eisenhutten.*, 6, 155 (1932).
29. G. R. Wallwork and A. Z. Hed, *Oxid. Met.*, 3, 171, 213, 229 and 243 (1971).
30. W. H. Gitzen, Editor, ' $\text{Al}_2\text{O}_3$  as a Ceramic Material,' Amer. Ceram. Soc., Pub. No. 4 (1970).
31. F. S. Gallasso, 'Structure and Properties of Inorganic Solids,' Int. Series in Sol. St. Phys., Vol. 7 (1970).
32. F. A. Kröger, Proc. of NACE Conf. on 'High Temperature Corrosion', San Diego, California, March (1981).
33. K. A. Hay, Report RD/L/R 1673, Central Electricity Res. Lab., Leatherhead, England (1970).
34. R. Linder and Å. Åkertrøm, *Z. Phys. Chem., N. F.*, 6, 162 (1956).
35. W. C. Hagel and A. U. Seybolt, *J. Electrochem. Soc.*, 108, 1146 (1961).
36. W. C. Hagel, *J. Amer. Cer. Soc.*, 48, 70 (1965).
37. L. C. Walters and R. E. Grace, *J. Appl. Phys.*, 36, 2331 (1965).
38. Y. Oishi and W. D. Kingery, *J. Chem. Phys.*, 33, 480 (1960).
39. A. E. Paladino and W. D. Kingery, *ibid*, 37, 957 (1962).
40. K. P. R. Reddy and A. R. Cooper, Abstracts, Amer. Ceram. Soc. Bull., 55, 402 (1976) and 57, 306 (1978); quoted in Ref. (41).
41. D. J. Reed and B. J. Wuensch, *J. Amer. Ceram. Soc.*, 63, 88 (1980).
42. C. S. Giggins and F. S. Pettit, *Met. Trans.*, 2, 1071 (1971).
43. W. C. Hagel, P. L. Jorgensen and D. S. Tomalin, *J. Amer. Cer. Soc.*, 49, 23 (1966).
44. P. D. Ownby and G. E. Jungquist, *ibid*, 55, 433 (1971).
45. J. W. Halloran and H. U. Anderson, *ibid*, 57, 150 (1974).
46. J. M. Neve and R. L. Coble, *ibid*, 57, 274 (1974).
47. H. A. Wang and F. A. Kröger, *ibid*, 63, 613 (1980).
48. J. K. Tien and F. S. Pettit, *Met. Trans.*, 3, 1587 (1972).



49. K. P. R. Reddy, J. L. Smialek and A. R. Cooper, submitted to Oxid. Met., preprint furnished by the authors.
50. D. J. Young and M. Cohen, J. Electrochem. Soc., 124, 769 and 775 (1977).
51. J. L. Smialek, Met. Trans., 9A, 309 (1978).
52. H. Hindam and W. W. Smeltzer, J. Electrochem. Soc., 127, 1630 (1980).
53. E. J. Felten and F. S. Pettit, Oxid. Met., 10, 189 (1976).
54. J. S. Sheasby and D. B. Jory, *ibid*, 12, 527 (1978).
55. D. Caplan, A. Harvey and M. Cohen, Corros. Sci., 3, 161 (1963).
56. D. Caplan and G. I. Sproule, Oxid. Met., 9, 459 (1975).
57. T. Homma, H. Hindam, Y. Pyun and W. W. Smeltzer, in press.
58. D. Mortimer and M. L. Post, Corros. Sci., 8, 499 (1968).
59. K. P. Lillerud and P. Kofstad, J. Electrochem. Soc., 127, 2397 (1980).
60. F. A. Golightly, F. H. Stott and G. C. Wood, Oxid. Met., 10, 163 (1976).
61. F. A. Golightly, F. H. Stott and G. C. Wood, J. Electrochem. Soc., 126, 1035 (1979).
62. F. A. Golightly, G. C. Wood and F. H. Stott, Oxid. Met., 14, 217 (1980).
63. D. G. Barnes, J. M. Clavert, K. A. Hay and D. G. Lees, Phil. Mag., 28, 1303 (1973).
64. D. G. Lees and J. M. Calvert, Corros. Sci., 16, 767 (1976).
65. Y. Ikeda and K. Nii, Oxid. Met., 12, 487 (1978).
66. J. Stringer and I. G. Wright, *ibid*, 5, 59 (1972).
67. I. G. Wright and B. A. Wilcox, *ibid*, 8, 283 (1974).
68. O. T. Goncel, J. Stringer and D. P. Whittle, Corros. Sci., 18, 701 (1978).
69. H. Hindam and D. P. Whittle, submitted to J. Electrochem. Soc.
70. C. S. Giggins and F. S. Pettit, Report ARL 75-0234, Pratt and Whitney Aircraft, Connecticut (1975).
71. J. D. Kuenzly and D. L. Douglass, Oxid. Met., 8, 139 (1974).
72. A. Kumar, M. Hasrallah and D. L. Douglass, *ibid*, 8, 227 (1974).
73. J. Stringer, I. M. Allam and D. P. Whittle, Thin Sol. Films, 45, 377 (1977).
74. I. M. Allam, D. P. Whittle and J. Stringer, Oxid. Met., 12, 35 (1978).

75. I. M. Allam, Ph.D. Thesis, University of Liverpool (1979).
76. I. M. Allam, D. P. Whittle and J. Stringer, *Oxid. Met.*, 13, 381 (1979).
77. J. L. Smialek, NASA Technical Memorandum 81676, Cleveland, Ohio (1981).
78. H. Hindam, 'Microstructure and Growth of  $Al_2O_3$  on Ni-Al Alloys', Ph.D. Thesis, McMaster University, Hamilton, Ont. (1979).
79. H. Hindam and D. P. Whittle, in preparation.
80. J. Stringer, A. Z. Hed, G. R. Wallwork and B. A. Wilcox, *Corros. Sci.*, 12, 625 (1972).
81. H. E. Evans, D. A. Hilton, R. A. Holm and S. J. Webster, *Oxid. Met.*, 12, 473 (1978).
82. H. Hindam and D. P. Whittle, *J. Electrochem. Soc.*, 129, 1147 (1982).
83. J. Markali, in 'Mechanical Properties of Engineering Ceramics', W. W. Kriegel and H. Palmour, Editors, Interscience, New York (1961).
84. D. J. Barber, *Phil. Mag.*, 10, 75 (1964).
85. E. A. Gulbransen, *Mém. Sci. Rev. Mét.*, 62, 253 (1965).
86. R. L. Tallman and E. A. Gulbransen, *J. Electrochem. Soc.*, 114, 1227 (1967).
87. G. C. Wood and T. Hodgkiess, *ibid*, 113, 319 (1966).
88. G. C. Wood and D. P. Whittle, *ibid*, 115, 126 and 133 (1968).
89. H. W. Paxton and E. J. Pasierb, *Trans. AIME*, 218, 794 (1960).
90. D. M. Poole and P. M. Thomas, *J. Inst. Met.*, 90, 228 (1962).
91. C. S. Tedmon, Jr., *J. Electrochem. Soc.*, 114, 788 (1967).
92. D. P. Whittle, D. J. Evans, D. B. Scully and G. C. Wood, *Acta Met.*, 15, 1421 and 1747 (1967).
93. H. E. Evans, D. A. Hilton and R. A. Holm, *Oxid. Met.*, 10, 149 (1976).
94. J. C. Killeen, A. F. Smith and R. K. Wild, *Corros. Sci.*, 16, 551 (1976).
95. B. D. Bastow, D. P. Whittle and G. C. Wood, *Oxid. Met.*, 12, 413 (1978).
96. T. Hodgkiess, G. C. Wood, D. P. Whittle and B. D. Bastow, *ibid*, 12, 439 (1978).
97. G. C. Wood and D. P. Whittle, *Corros. Sci.*, 4, 263 and 293 (1964).
98. G. C. Wood, T. Hodgkiess and D. P. Whittle, *ibid*, 6, 129 (1966).

99. G. C. Wood and D. P. Whittle, *ibid*, 7, 763 (1967).
100. M. M. P. Janssen, *Met. Trans.*, 4, 1623 (1973).
101. F. N. Rhines and J. S. Wolf, *ibid*, 1, 1701 (1970).
102. V. R. Howes, *ibid*, 8, 221 (1968) and *ibid*, 10, 99 (1970).
103. V. R. Howes, *J. Electrochem. Soc.*, 116, 1286 (1969).
104. C. S. Giggins, B. H. Kear, F. S. Pettit and J. K. Tien, *Met. Trans.*, 5, 1685 (1974).
105. B. W. Dunnington, F. H. Beck and M. G. Fontana, *Corros.*, 8, 2t (1952).
106. G. B. Gibbs and R. Hales, *Corros. Sci.*, 17, 487 (1977).
107. G. B. Gibbs, *Oxid. Met.*, 16, 147 (1981).
108. B. Lustman, *Trans. Met. Soc. AIME*, 188, 995 (1950).
109. J. E. Antill and K. A. Peakall, *J. Iron and Steel Inst.*, 1136, Nov. (1967).
110. C. E. Lowell, D. L. Deadmore, S. J. Grisaffe and I. L. Drell, NASA TN D-6290, Lewis Research Center, Cleveland, Ohio, April (1971).
111. H. Nagai, M. Okabayashi and H. Mitani, *Trans. JIM*, 21, 341 (1980).
112. C. A. Barrett, A. S. Kahn and C. E. Lowell, *J. Electrochem. Soc.*, 128, 25 (1981).
113. P. Kofstad, 'Nonstoichiometry, Diffusion and Electrical Conductivity in Binary Metal Oxides', Wiley-Interscience, New York (1972).
114. M. M. El-Aiat and F. A. Kröger, *J. Am. Ceram. Soc.* 65, 280 (1982).
115. J. C. Pivin, C. Roques-Carmes, P. Moulin, A. M. Huntz and P. Lacombe, *Mém. Sci. Rev. Mét.*, 75, 639 (1978).
116. E. Tsuzi, *Met. Trans.*, 11A, 1965 (1980).
117. M. Sakiyama, P. Tomaszewicz and G. R. Wallwork, *Oxid. Met.*, 13, 311 (1979).
118. J. C. Pivin, D. Delaunay, A. M. Huntz and P. Lacombe, *Corros. Sci.*, 20, 351 (1980).
119. J. Stringer, *Met. Rev.*, 11, 113 (1966).
120. H. Hindam and W. W. Smeltzer, *J. Electrochem. Soc.*, 127, 1622 (1979).
121. H. Hindam and D. P. Whittle, submitted to *J. Mat. Sciences*.
122. H. Hindam and D. P. Whittle, in preparation.

123. C. A. Phalnikar, E. B. Evans and W. M. Baldwin, J. Electrochem. Soc., 103, 429 (1956).
124. E. A. Gulbransen and K. F. Andrew, *ibid*, 104, 334 (1957).
125. W. C. Hagel, Trans. ASM, 56, 583 (1963).
126. L. Cadiou and J. Paidassi, Mém. Sci. Rev. Métal., 66, 217 (1969).
127. C. S. Giggins and F. S. Pettit, Trans. Met. Soc. AIME, 245, 2495 (1969).
128. D. Caplan and M. Cohen, J. Electrochem. Soc., 108, 438 (1961).
129. H. C. Graham and H. H. Davis, J. Amer. Ceramic Soc., 54, 89 (1971).
130. C. A. Stearns, F. J. Kohl and G. C. Fryburg, J. Electrochem. Soc., 121, 945 (1974).
131. C. E. Lowell and W. A. Sanders, Oxid. Met., 5, 221 (1972).
132. D. R. Tenney, C. T. Young and H. W. Herring, Met. Trans., 5, 1001 (1974).
133. C. T. Young, D. R. Tenney and H. W. Herring, Met. Trans. A, 6A, 2253 (1975).
134. G. C. Fryburg, F. J. Kohl and C. A. Stearns, J. Electrochem. Soc., 121, 952 (1974).
135. Y. W. Kim and G. R. Belton, Met. Trans., 5, 1811 (1974).
136. G. C. Fryburg, R. A. Miller, F. J. Kohl and C. A. Stearns, J. Electrochem. Soc., 124, 1738 (1977).
137. G. M. Ecer and G. H. Meier, Oxid. Met., 13, 119 (1979).
138. S. Espevik, R. A. Rapp, P. L. Daniel and J. P. Hirth, *ibid*, 14, 85 (1980).
139. T. Hodgkiess, G. C. Wood, D. P. Whittle and B. D. Bastow, *ibid*, 14, 85 (1980).
140. P. Moulin, A. M. Huntz and P. Lacombe, Acta Met., 28, 745 (1980).
141. E. J. Felten, J. Electrochem. Soc., 108, 490 (1961).
142. J. M. Francis and W. H. Whitlow, Corros. Sci., 5, 701 (1965).
143. G. C. Wood and D. P. Whittle, *ibid*, 7, 763 (1967).
144. D. P. Whittle, M. E. El-Dahshan, and J. Stringer, *ibid*, 17, 879 (1977).
145. H. H. Davis, H. C. Graham and I. A. Kvernes, Oxid. Met., 3, 431 (1971).
146. I. G. Wright, B. A. Wilcox and R. I. Jaffee, *ibid*, 9, 275 (1975).
147. H. T. Michels, Met. Trans., 7A, 379 (1976).

148. G. C. Wood and J. Boustead, Corros. Sci., 8, 719 (1968).
149. O. T. Goncel, D. P. Whittle and J. Stringer, Oxid. Met., 15, 287 (1981).
150. H. Nagai, Y. Takebayashi and H. Mitani, Met. Trans., 12A, 435 (1981).
151. T. Amano, S. Yajima and Y. Saito, Trans. JIM, 20, 431 (1979).
152. F. S. Pettit, Trans. Met. Soc. AIME, 239, 1296 (1967).
153. C. S. Giggins and F. S. Pettit, J. Electrochem. Soc., 118, 1782 (1971).
154. A. S. Kahn, C. E. Lowell and C. A. Barrett, *ibid*, 127, 671 (1980).
155. C. S. Wukusick and J. F. Collins, Mat. Res. and Stand., 633 (1964).
156. C. Wagner, Z. Phys. Chem., B21, 25 (1933); *ibid*, in 'Atom-Movements,' ASM Publication, Ohio, p.153 (1951).
157. W. W. Smeltzer and D. J. Young, Prog. Sol.-St. Chem., 10, Part(1), 17 (1975).
158. J. F. Elliot and M. Gleiser, Editors, 'Thermochemistry for Steel Making', Addison-Wesley, New York (1960).
159. K. P. R. Reddy, Ph.D. Thesis, Case Western Reserve University, Cleveland, Ohio (1979), quoted in Ref. (77).

# FIGURE CAPTIONS

- Figure 1. Schematic reaction kinetics for a protective scale forming alloy indicating the various stages of oxidation.
- Figure 2. Isothermal section at 1000°C in the Ni-Al-O phase diagram, after Elrefaie and Smeltzer<sup>(4)</sup>.
- Figure 3. Oxide map for Ni-Cr-Al system, after Wallwork and Hed<sup>(29)</sup>. Typical Ni-based superalloys and coating compositions are indicated.
- Figure 4. Tracer diffusion data of the mobile species in  $\text{Cr}_2\text{O}_3$  and  $\text{Al}_2\text{O}_3$ .
- Figure 5. Oxide ridge formation:
- a. pure Cr, after Caplan et al.<sup>(55)</sup>;
  - b.  $\beta$ -NiAl, after Hindam and Smeltzer<sup>(52)</sup>.
- Figure 6. Fracture section of the protective scales:
- a.  $\text{Cr}_2\text{O}_3$  on pure Cr<sup>(69)</sup>;
  - b.  $\text{Al}_2\text{O}_3$  on Co-15 Cr-8 Al, after Allam<sup>(75)</sup>.
- Figure 7. Convulsed scales:
- a.  $\text{Cr}_2\text{O}_3$  on pure Cr, after Caplan and Sproule<sup>(56)</sup>;
  - b.  $\text{Al}_2\text{O}_3$  on Fe-10 Al-3 Cu<sup>(79)</sup>.
- Figure 8. Cavity formation at the scale/alloy interface:
- a. Fe-25 Cr;
  - b. Co-10 Cr-11 Al, after Allam<sup>(75)</sup>.
- Figure 9. Effect of active element additions on the adherence of  $\text{Al}_2\text{O}_3$  scale:
- a. Fracture section of the detached scale formed on a Fe 10 Al 1 Cu Alloy<sup>(79)</sup>;
  - b. Deeply-etched section of the tenacious scale formed on a Fe-10Al-1Hf, illustrating the development of inwardly growing pegs<sup>(82)</sup>.

Figure 10. Arrhenius plot of reported parabolic rate constants for the oxidation of pure Cr (Refer to Table I).

Figure 11. Arrhenius plot of reported parabolic rate constants for the growth of  $\text{Cr}_2\text{O}_3$  on binary Cr-containing alloys (Refer to Table II).

Figure 12. Arrhenius plot of reported parabolic rate constants for the growth of  $\text{Cr}_2\text{O}_3$  on alloys containing active elements or dispersed oxides superimposed on the scatter band for binary alloys (Figure 11). (Refer to Table III.)

Figure 13. Arrhenius plot of reported 'apparent' parabolic rate constants for the growth of  $\text{Al}_2\text{O}_3$  on Al-containing alloys (Refer to Table IV).

Figure 14. Dependence of  $\text{Cr}_2\text{O}_3$  growth rate on  $P_{\text{O}_2}$ . Calculated values based on vacancy and interstitial mechanisms along with experimental values<sup>(69)</sup>.

Figure 15. Comparison of the parabolic growth constants for  $\text{Cr}_2\text{O}_3$  with diffusion data (see text for details).

Figure 16. Comparison of the apparent parabolic growth constants for  $\text{Al}_2\text{O}_3$  with diffusion data (see text for details).

## LIST OF TABLES

- Table I. Reference list and experimental conditions of the kinetic data for the oxidation of pure chromium.
- Table II. Reference list and experimental conditions of the growth kinetics of  $\text{Cr}_2\text{O}_3$  on binary chromium alloys.
- Table III. Reference list and experimental conditions of the growth kinetics of  $\text{Cr}_2\text{O}_3$  on chromium alloys containing oxygen-active elements.
- Table IV. Reference list and experimental conditions for the growth kinetics of  $\text{Al}_2\text{O}_3$  on Al-containing alloys.



TABLE I

Authors	Symbol	Atmosphere; $P_{O_2}$ (atm); Gas Flow	Vaporization of $Cr_2O_3$	Sample Surface Preparation
Phalnikar et al. <sup>(123)</sup>	⊙	$O_2$ ; 1.0	UC	MP
Gulbransen and Andrew <sup>(124)</sup>	⊙	$O_2$	UC	MP
Hagel <sup>(125)</sup>	Δ	$O_2$ ; 0.1	UC but evaluated	MP
Caplan et al. <sup>(55,56)</sup>	▽ ■ ▲ ▼	$O_2$ ; 1.0; F	S	EP EP+E TGA TM
Mortimer and Post <sup>(58)</sup>	◇ ●	$O_2$ ; 1.0; F 10ml/min.	UC	EP+E
Cadiou and Paidassi <sup>(126)</sup>	□	$O_2$ ; 1.0; F 100ml/min.	C*	MP+A
Giggins and Pettit <sup>(127)</sup>	●	$O_2$ ; 0.1	UC	MP
Lillerud and Kofstad <sup>(59)</sup>	○	$O_2$ ; 1.0; F	C	MP+A
Hindam and Whittle <sup>(69)</sup>	Δ	$CO/CO_2$ ; $10^{-14}$ → $10^{-8}$ (at 1000°C); 0.3 cm/sec.	Insignificant	MP

F = Flow; S = Static; C = Corrected; C\* = Corrected using data of Ref (125);

UC = Uncorrected; S = Suppressed; MP = Mechanically polished;

E = Electropolished; E = Etched; CE = Cathodically etched; A = Annealed;

TGA = Thermogravimetric data; TM = Thickness measurement data.

TABLE II

Authors	Alloy Composition; Symbol	Atmosphere; $P_{O_2}$ (atm); Gas Flow	Scale Composition	Vaporization of $Cr_2O_3$	Sample Surface Preparation
Phalnikar et al. (123)	Co38.3Cr ★ Co48.5Cr ★	Air	Exclusively $Cr_2O_3$	UC	MP
Giggins and Pettit (127)	Ni30Cr ▲ Ni40Cr ▼	$O_2$ ; 0.1	Predominantly $Cr_2O_3$ ; Trace $NiAl_2O_4$ ; $Cr_2O_3$ Int. Prec.	UC	EP MP
Ecer and Meier (137)	Ni44Cr ● Ni50Cr ●	$O_2$ ; 1.0	$Cr_2O_3$ (Ni~2wt. %); Transient NiO; $Cr_2O_3$ Int. Prec.	UC but evaluated	MP
Espevik et al. (138)	Ni30Cr ●	Air	$Cr_2O_3$	UC	MP
Hodgkiess et al. (139)	Ni40Cr ◆ Ni70Cr ■	$O_2$ ; 1.0; F	$Cr_2O_3$ +Ni-rich Phases; $Cr_2O_3$ (Ni~0.5 wt.%) $Cr_2O_3$ Int. Prec.	S	MP+CE
Moulin et al. (140)	Ni30Cr ● Ni40Cr ●	$O_2$ ; 1.0	$Cr_2O_3$	C*	EP+A
Wallwork and Zed (29)	Ni30Cr ●	$O_2$ ; 0.13; F	Mainly $Cr_2O_3$ ; $NiCr_2O_4$ ; unidentified phase	UC, $Cr_2O_3$ deposits on suspension wire	MP
Felten (141)	Fe25Cr ○ Fe37.5Cr ○	$O_2$ ; 0.13	$Cr_2O_3$ (single phase)	UC	MP

TABLE II (continued)

Authors	Alloy Composition Symbol	Atmosphere; $P_{O_2}$ (atm); Gas Flow	Scale Composition	Vaporization of $Cr_2O_3$	Sample Surface Preparation
Francis and Whitlow <sup>(142)</sup>	Fe25Cr $\odot$	$CO_2$ ; F 0.8 cm/sec.	$Cr_2O_3$	UC	-
Tedmon <sup>(91)</sup>	Fe25Cr $\Delta$ Fe30Cr $\nabla$ Fe40Cr $\Delta$ Fe45Cr $\nabla$ Fe50Cr $\odot$ Fe60Cr $\odot$ Fe70Cr $\odot$ Fe95Cr $\diamond$	$O_2$ ; 0.13	$Cr_2O_3$ ( $Fe_2O_3$ < 1 wt.%)	UC	MP
Wood and Whittle <sup>(143)</sup>	Fe14Cr $\square$ Fe27.4Cr $\diamond$	$O_2$ ; 1.0	(Cr, Fe) $_2O_3$ (~ 2 wt % Fe)	S	MP
Ibid <sup>(88)</sup>	Fe59.5Cr $\square$		(Cr, Fe) $_2O_3$ (~ 0.8 wt %)		
Mortimer and Post <sup>(58)</sup>	Fe50Cr $\odot$	$O_2$ ; 1.0; F 10ml/min.	(Cr, Fe) $_2O_3$ (~ 2 wt % Fe)	UC	EP+E

F = Flow; S = Static; C = Corrected; C\* = Corrected using data of Ref (125);

UC = Uncorrected; S = Suppressed; MP = Mechanically polished;

E = Electropolished; E = Etched; CE = Cathodically etched; A = Annealed;

TGA = Thermogravimetric data; TM = Thickness measurement data.

TABLE III

Authors	Alloy Composition; Symbol	Atmosphere; $P_{O_2}$ (atm); Gas Flow	Scale Composition	Vaporization of $Cr_2O_3$	Sample Surface Preparation
Stringer and Wright <sup>(66)</sup>	Co21Cr-3v% $Y_2O_3$ ★	$O_2$ ; 0.13; F	$Cr_2O_3$	C*	MP
Whittle et al. <sup>(144)</sup>	Co10Cr-1Ti ☆ Co10Cr-1Zr ★ Co10Cr-1Hf ☆ Co15Cr-1Ti ☆ Co15Cr-1Zr ★ Co15Cr-1Hf ☆ (Pre-oxidized in $Cr/Cr_2O_3$ packs)	$O_2$ ; 1.0; F or Air	Mainly $Cr_2O_3$ ; UC Transient CoO; $Cr_2O_3$ Int. Prec.		MP
Giggins and Pettit <sup>(42)</sup>	Ni20Cr-2v% $ThO_2$ ●	$O_2$ ; 0.1; S	Mainly $Cr_2O_3$	C*	MP
Davis et al. <sup>(145)</sup>	Ni33.7Cr- 1 $ThO_2$ ●	$O_2$ ; 0.2; F12cm/sec.	$Cr_2O_3$	UC but evaluated	MP
Stringer et al. <sup>(17)</sup>	Ni20Cr-3v% $Y_2O_3$ ■ Ni20Cr-3v% $CeO_2$ ◆	$O_2$ ; 0.13; F	Essentially $Cr_2O_3$ ; Trace $NiCr_2O_4$	-	MP
Wright et al. <sup>(146)</sup>	Ni20Cr-3v% $Y_2O_3$ ●	$O_2$ ; 0.13; F	$Cr_2O_3$ ; Trans- ient NiO, $NiCr_2O_4$	UC	MP
Michels <sup>(147)</sup>	Ni20Cr-0.04 $Y_2O_3$ ▲ Ni20Cr-0.02 $La_2O_3$ ▼ Ni20Cr-1.27 $Li_2O$ ●	Air; F 0.42cm/sec	$Cr_2O_3$ ; Trace NiO, $NiCr_2O_4$	UC	MP

TABLE III (continued)

Authors	Alloy Composition Symbol	Atmosphere; $P_{O_2}$ (atm); Gas Flow	Scale Composition	Vaporization of $Cr_2O_3$	Sample Surface Preparation
Felten <sup>(141)</sup>	Fe25Cr-1Y $\Delta$	$O_2$ ; 0.13	$Cr_2O_3(Y_2O_3$	UC	MP
			+ $YCrO_3$ )		
	Fe37.5Cr-1Y $\nabla$		$Cr_2O_3(Y_2O_3$		
			+ $YCrO_3$ )		
	Fe25Cr-1.6La $\Theta$		$Cr_2O_3(La_2O_3$		
			+ $LaCrO_3$ )		
	Fe25Cr-1.8Gd $\Theta$		$Cr_2O_3(Gd_2O_3$		
	Fe25Cr-1.8Dy $\Delta$		$Cr_2O_3(Dy_2O_3$		
	Fe25Cr-1.9Er $\nabla$		$Cr_2O_3(Er_2O_3$		
Francis and Whitlow <sup>(142)</sup>	Fe25-1Y $\square$	$CO_2$ ; F 0.8cm/sec.	$Cr_2O_3(Y_2O_3$ + Y-rich Int. Prec.)	UC	-
Wood and Boustead <sup>(148)</sup>	Fe27.7Cr-0.8Y $\Theta$	$O_2$	$Cr_2O_3(Fe \sim 0.5$ wt%, $Y \sim 0.6$ wt %); Y-rich Int. Prec.	S	EP+CE
Wright and Wilcox <sup>(67)</sup>	Fe16Cr-3v% $Y_2O_3$ $\diamond$	$O_2$ ; 0.13; F	$Cr_2O_3$ (Trace Fe)	UC	MP
	Fe18Cr-0.1Y $\square$				
	Fe16Cr-0.5Zr $\diamond$		$Cr_2O_3$ (Int.Prec.)		
Goncel et al. <sup>(149)</sup>	Fe14Cr-1Hf $\Theta$	$O_2$ ; 1.0; F	$Cr_2O_3(HfO_2$	UC	MP
	Fe14Cr-1Ti $\Theta$		dispersoids		
	Fe18Cr-1Hf $\Theta$		or $TiO_2$ sub-		
	Fe18Cr-1Ti $\Theta$		surface layer)		
	Pre-oxidized in $Cr/Cr_2O_3$				
	Packs				

TABLE III (continued)

Authors	Alloy Composition Symbol	Atmosphere; $P_{O_2}$ (atm); Gas Flow	Scale Composition	Vaporization of $Cr_2O_3$	Sample Surface Preparation
Nagai et al. (150)	$Fe_{20}Cr-1Y_2O_3$ ○	Air	$Cr_2O_3$ (~3.3 wt % % $Fe_2O_3$ + ~0.43 wt % $Y_2O_3$ )	UC	MP+A
	$Fe_{20}Cr-1La_2O_3$ ●		$Cr_2O_3$ (~2.7 wt % $Fe_2O_3$ + 0.33 wt % $La_2O_3$ )		

F = Flow; S = Static; C = Corrected; C\* = Corrected using data of Ref (125);

UC = Uncorrected; S = Suppressed; MP = Mechanically polished;

E = Electropolished; E = Etched; CE = Cathodically etched; A = Annealed;

TGA = Thermogravimetric data; TM = Thickness measurement data.

TABLE IV

Authors	Alloy Composition Symbol	Atmosphere; $P_{O_2}$ (atm)	Scale Composition	Remarks
Giggins and Pettit <sup>(70)</sup>	Co25Cr6Al $\diamond$ Ni16Cr6Al $\bullet$  Co25Cr6Al-0.1Y $\nabla$ Ni16Cr6Al-0.1Y $\blacklozenge$	Air	Al <sub>2</sub> O <sub>3</sub> (Transient NiO, CoO, NiCr <sub>2</sub> O <sub>4</sub> , CoCr <sub>2</sub> O <sub>4</sub> ) Al <sub>2</sub> O <sub>3</sub> (Y <sub>2</sub> O <sub>3</sub> , YA1O <sub>3</sub> )	TGA and TM Approximate Parabolic Kinetics - 100 hr.
Tien and and Pettit <sup>(48)</sup>	Fe25Cr4Al $\square$  Fe25Cr4Al-0.01 ~1% Y $\blacksquare$ Fe25Cr4Al-0.2Sc $\triangle$	O <sub>2</sub> ; 0.1 or Air	Al <sub>2</sub> O <sub>3</sub> (Transient Cr <sub>2</sub> O <sub>3</sub> )  Al <sub>2</sub> O <sub>3</sub> (YA1O <sub>3</sub> ) Al <sub>2</sub> O <sub>3</sub> (Sc <sub>2</sub> O <sub>3</sub> )	TGA Parabolic Kinetics ~24hr
Golightly et al. <sup>(60)</sup>	Fe27Cr4Al $\square$ Fe27Cr4Al-0.02 ~ 0.8Y	O <sub>2</sub> ; 1.0	Al <sub>2</sub> O <sub>3</sub> (Fe+Cr < 1 wt%)	TGA - ~ 24 hr
Amano et al. <sup>(151)</sup>	Fe20Cr4Al $\diamond$ Fe20Cr4Al(0.01, 0.04, 0.4 Ce)	Air	Al <sub>2</sub> O <sub>3</sub> (CeO <sub>2</sub> )	TGA Parabolic Kinetics - 100 hr.
Smialek <sup>(51)</sup>	Ni25Al $\nabla$	Air	Mostly Al <sub>2</sub> O <sub>3</sub>	TM Approximate Parabolic Kine- tics ~ 100 hr
Kuenzly and Douglass <sup>(71)</sup>	Ni13Al $\bullet$ Ni13Al-0.5Y	Air	Al <sub>2</sub> O <sub>3</sub> NiAl <sub>2</sub> O <sub>4</sub> (Y <sub>3</sub> Al <sub>5</sub> O <sub>12</sub> , Y <sub>2</sub> O <sub>3</sub> , YA1O <sub>3</sub> )	TGA Approximate Parabolic Kine- tics after a brief stage ~ 50 hr

TABLE IV. (continued)

Authors	Alloy Composition; Symbol	Atmosphere; $P_{O_2}$ (atm)	Scale Composition	Remarks
Pettit <sup>(152)</sup>	Ni25Al ○	$O_2$ ; 0.1	$Al_2O_3$ only	TGA Parabolic Kinetics ~ 20 hr
Hindam and Smeltzer <sup>(52)</sup>	Ni32Al ○	$O_2$ ; 1.0	$Al_2O_3$ (~0.5 Ni)	TM Non Parabolic Kinetics ~ 15d
Giggins and Pettit <sup>(153)</sup>	Ni5Cr6Al ◇ Ni20Cr6Al ●	$O_2$ ; 0.1	$Al_2O_3$ (trace dissolved Cr)	TGA Parabolic Kinetics ~ 20 hr
Kahn et al. <sup>(154)</sup>	Ni14Cr24Al-(0-1.13)Zr ○	Air	$Al_2O_3$ ( $ZrO_2$ )	TGA Parabolic Kinetics ~ 200 hr
Kumar et al. <sup>(72)</sup>	Ni10Cr5Al ▲ Ni10Cr5Al-0.5Y ▲ Ni10Cr5Al-1Th ▲	Air	$Al_2O_3$ $NiAl_2O_4$ ( $NiO, Y_2O_3$ $YAlO_3, Y_3Al_5O_{12}$ ) $NiAl_2O_4$ ( $ThO_2$ )	TGA Non Parabolic Kinetics ~ 60 hr.
Felten and Pettit <sup>(53)</sup>	Pt6Al ○	$CO/CO_2 = 1.3$	$Al_2O_3$	TM Parabolic Kinetics ~ 100 hr Deviation > 100 hr.
Sheasby and Jory <sup>(54)</sup>	Pt22Al ▼	Air; 0.15; F	$Al_2O_3$	TGA
Wukusick and Collins <sup>(155)</sup>	Fe25Cr4Al-1YΔ	Air; 1.0; S	$Al_2O_3$ ( $Y_2O_3$ )	TGA

F = Flow; S = Static; TGA = Thermogravimetric data; TM = Thickness measurement data.



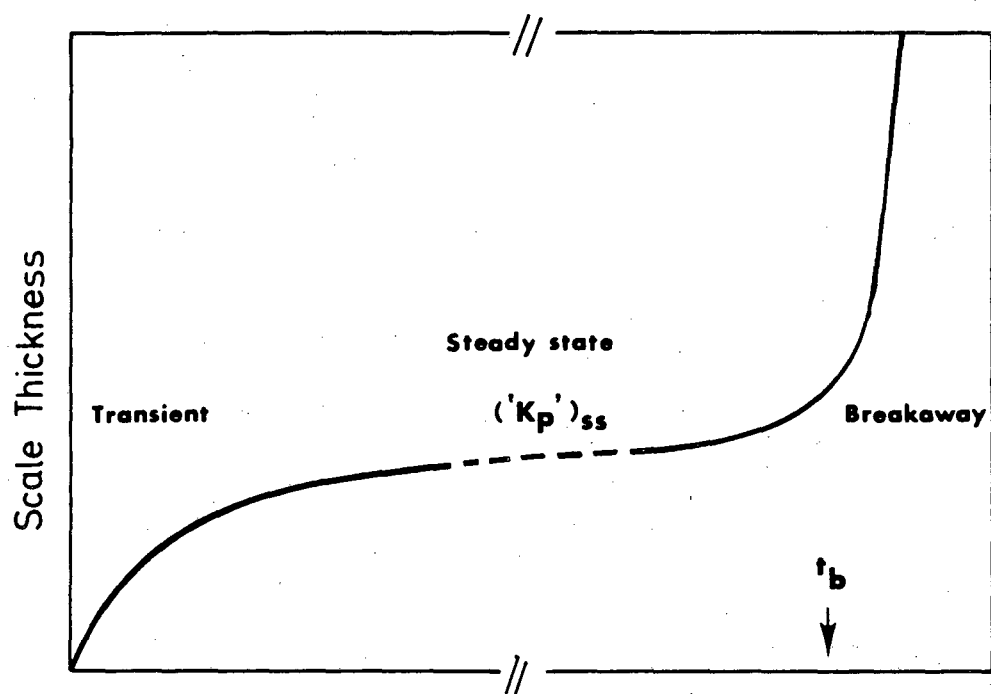
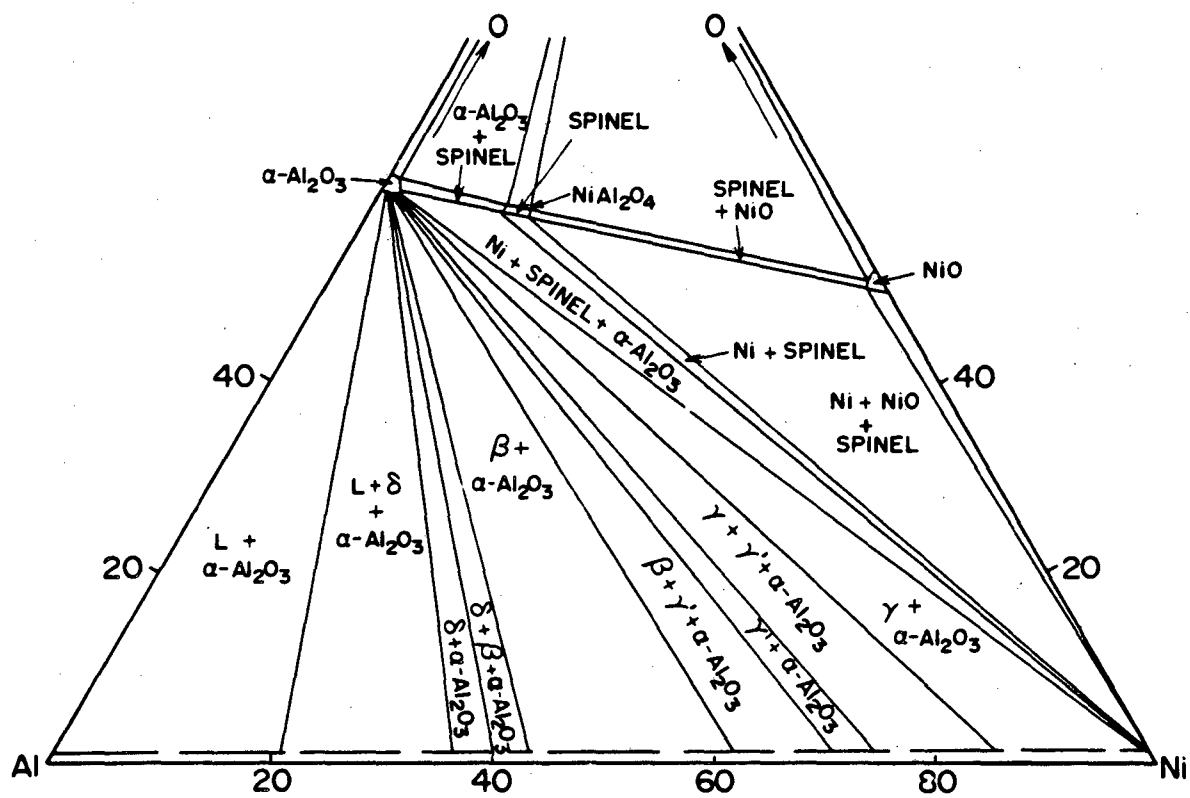


Figure 1.

Exposure Time

XBL 821-7734



**Ni-Al-O isotherm(1000°C)**  
**Elrefaie and Smeltzer**

Figure 2.

XBL 821-7650

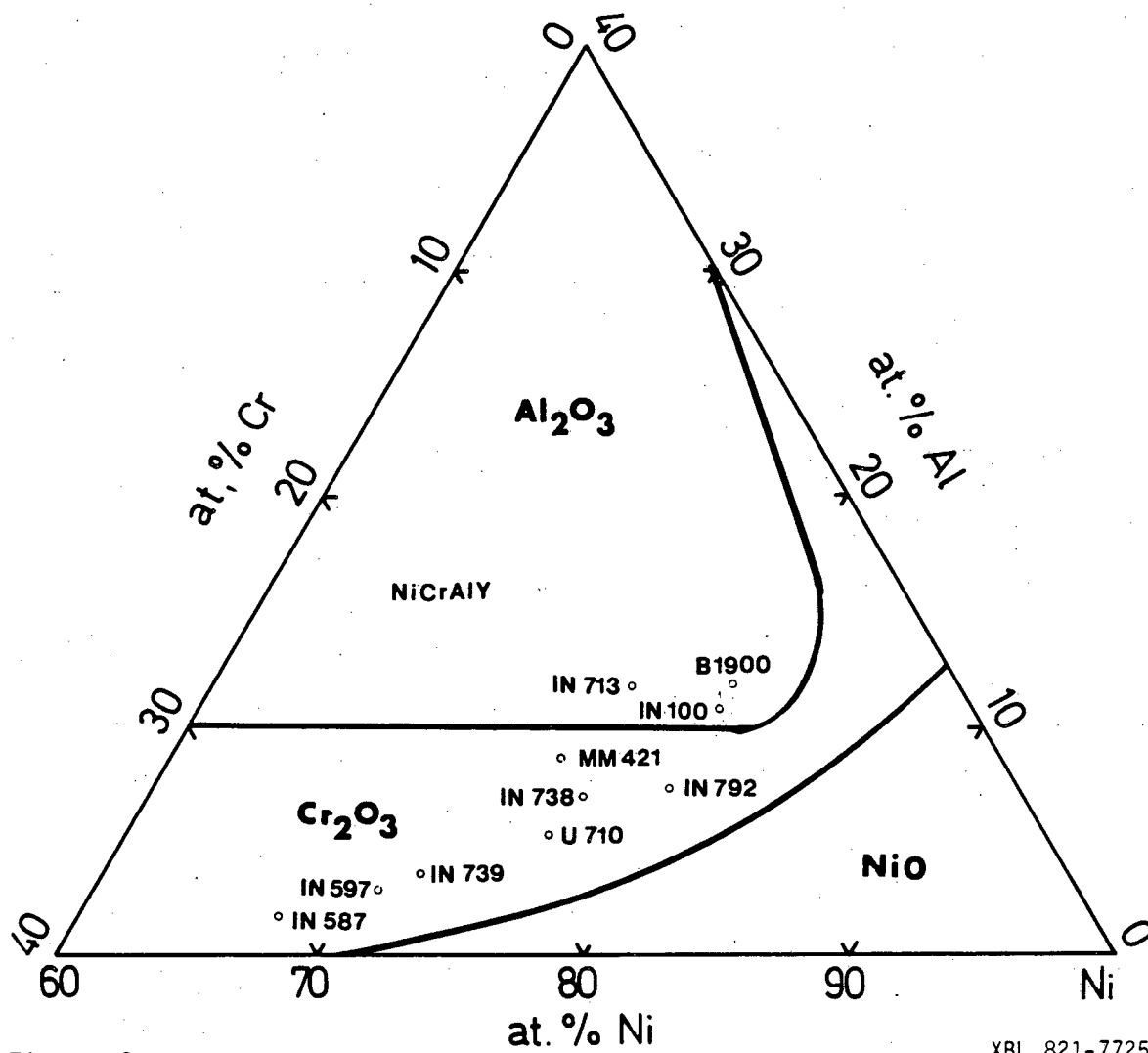


Figure 3.

XBL 821-7725

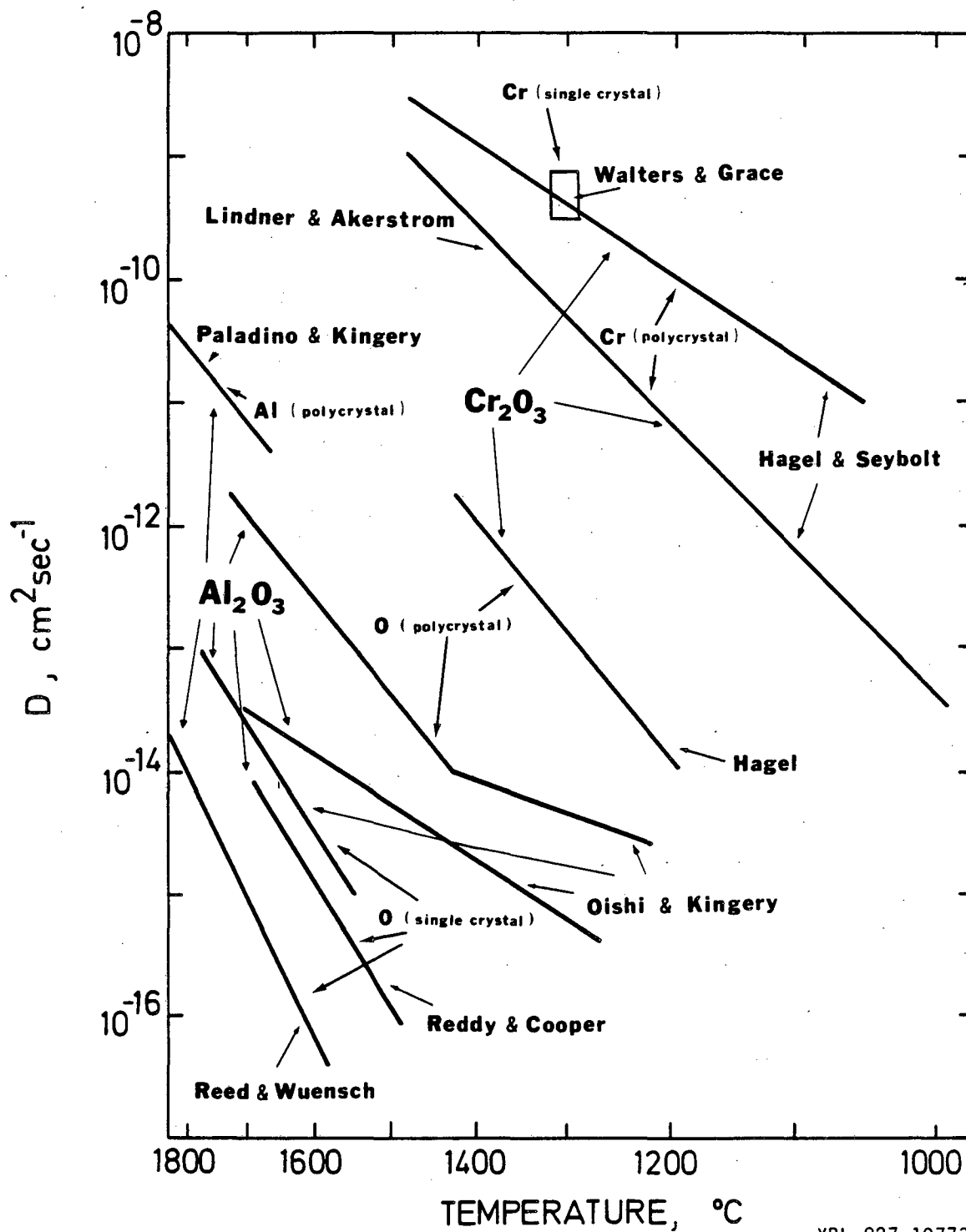
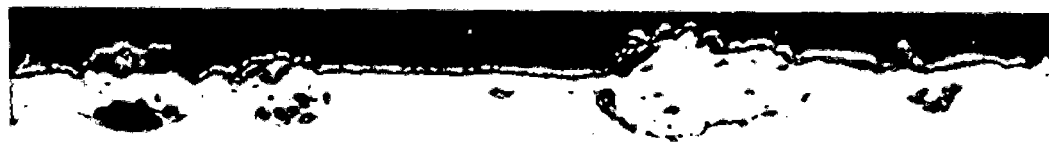
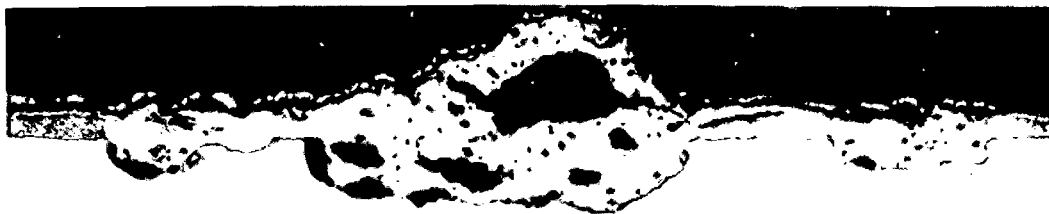


Figure 4.

XBL 827-10773



20 $\mu$



A

Cr — Caplan et al

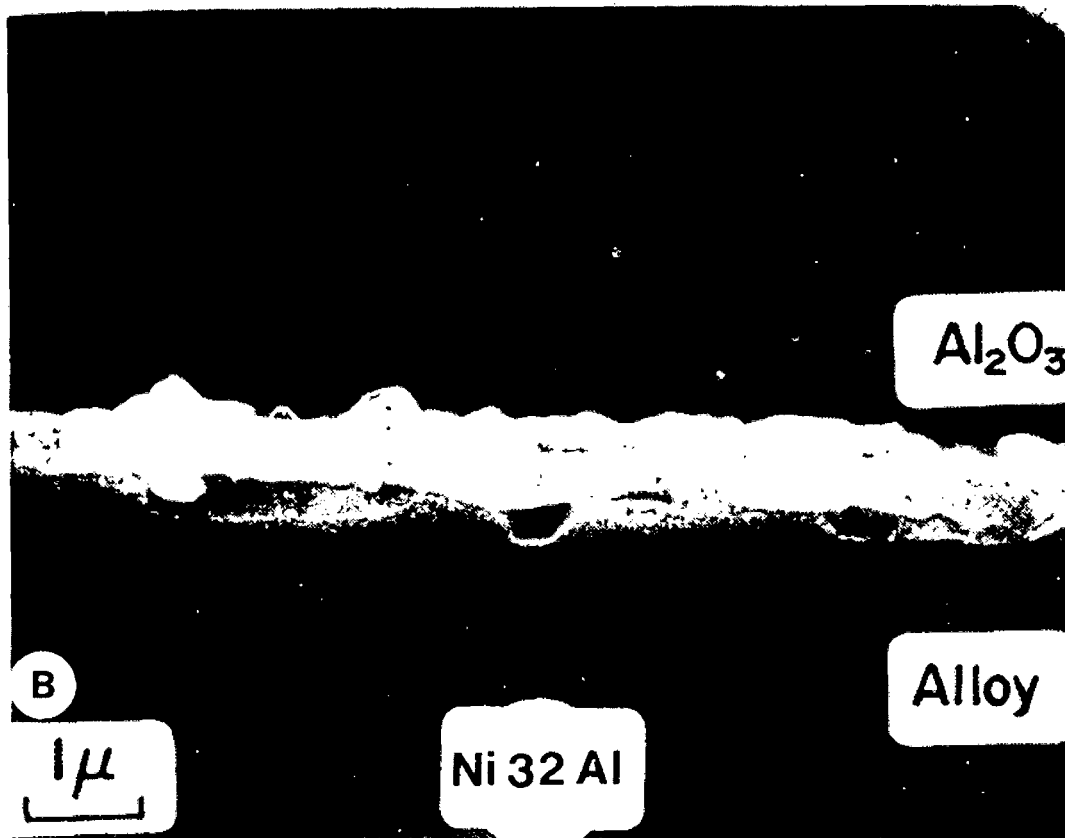


Figure 5.

XBB 821-265A

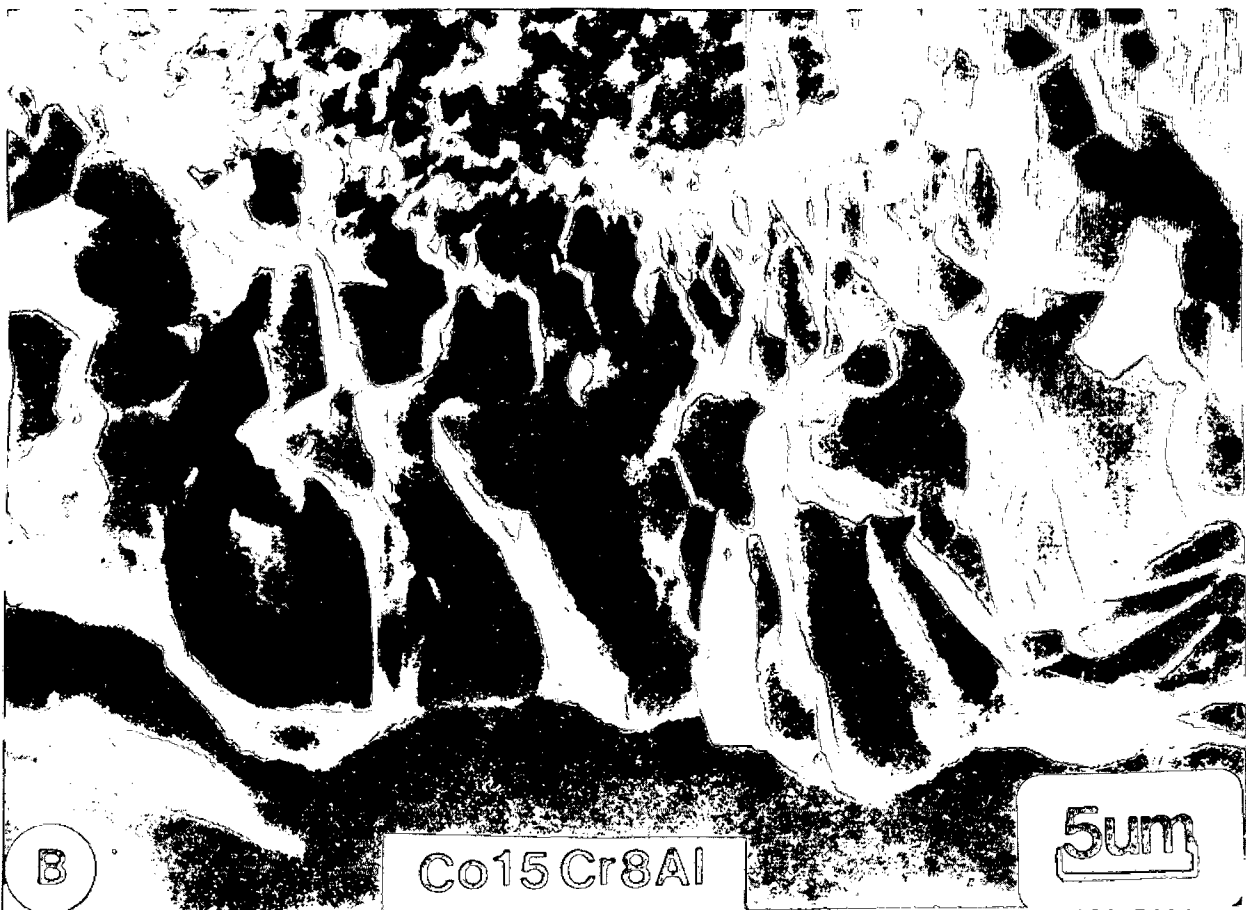
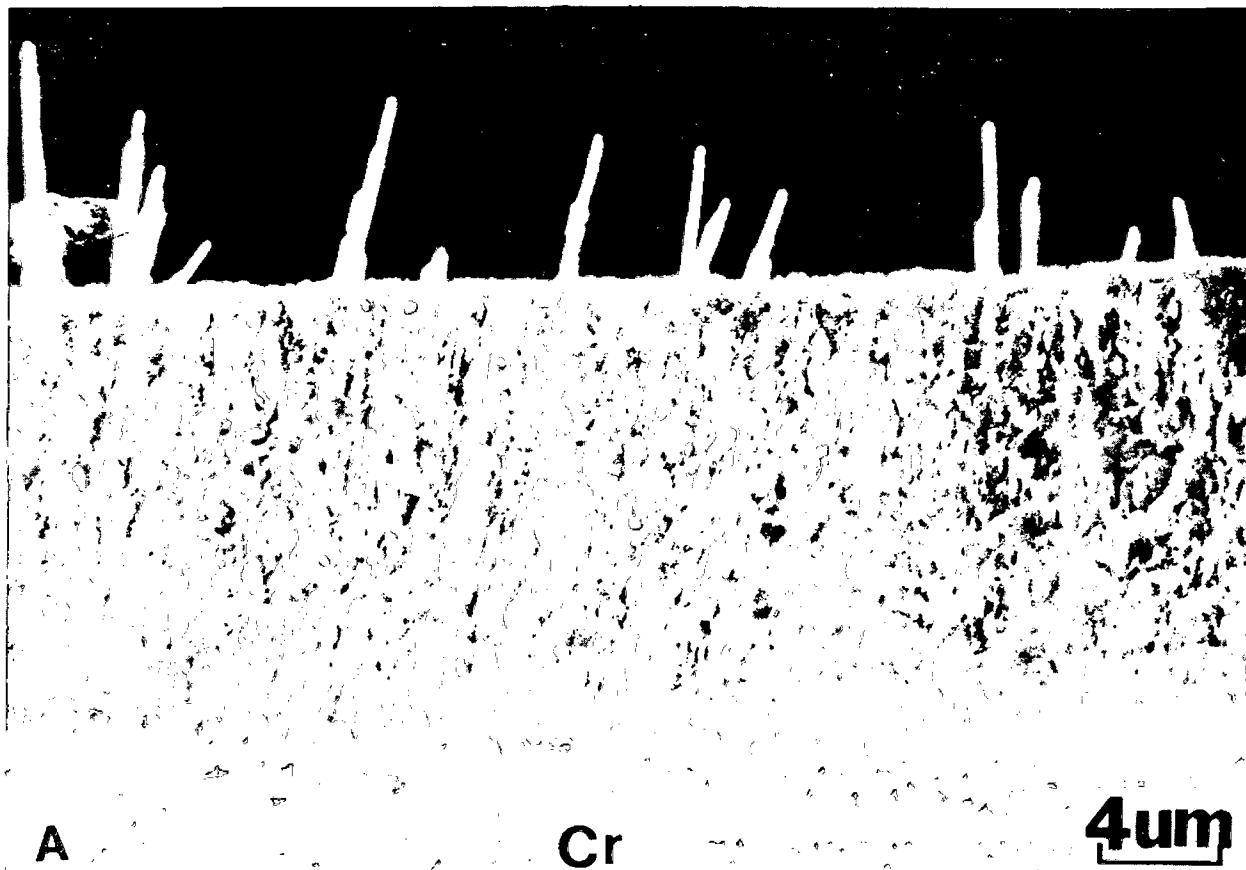
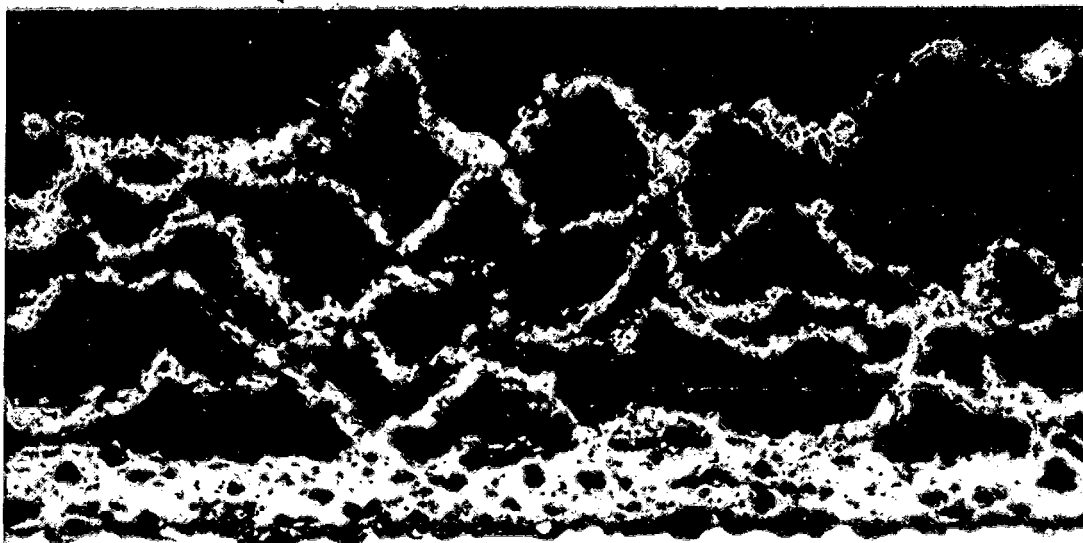


Figure 6.

XBB 828-7485



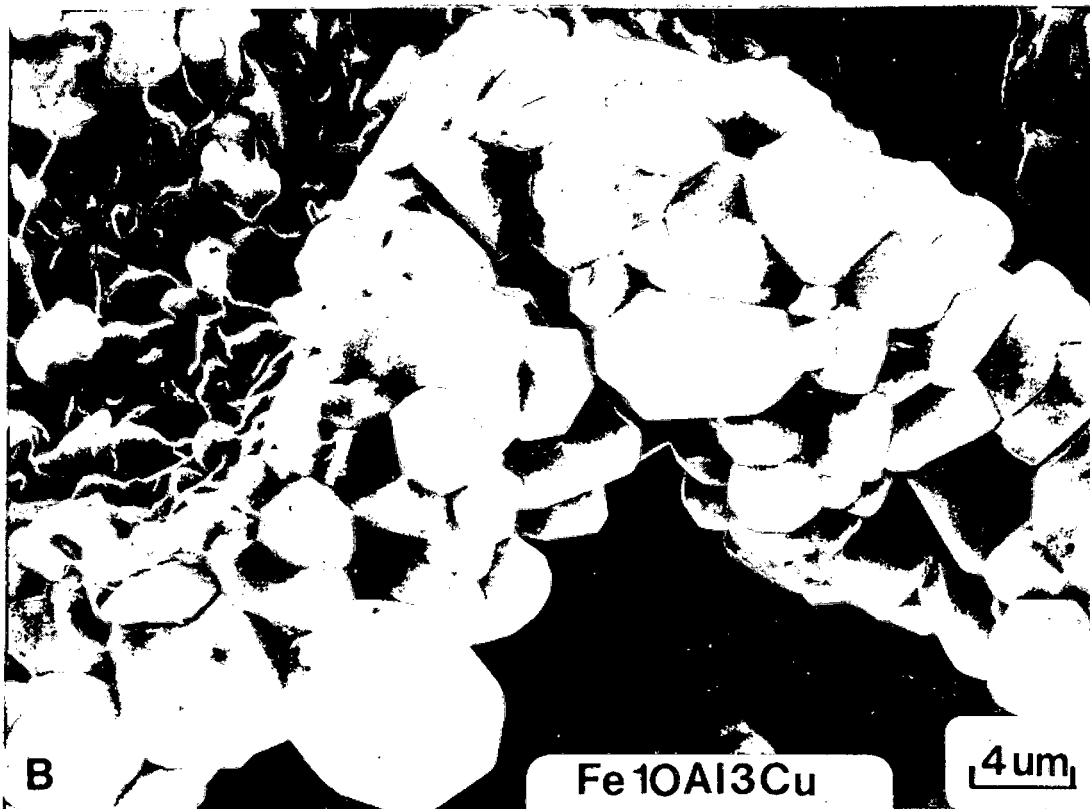
50 $\mu$



A

Cr - Caplan et al

20 $\mu$



B

Fe<sub>10</sub>Al<sub>3</sub>Cu

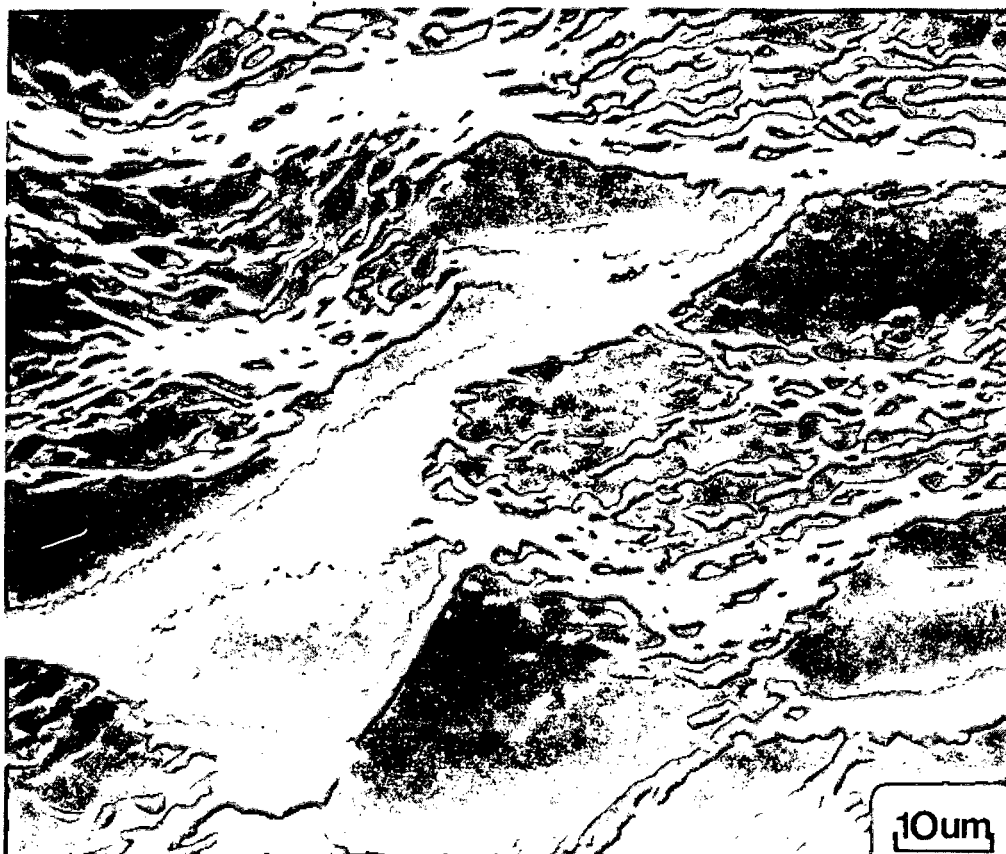
4 $\mu$

Figure 7.

XBB 828-7487



**A** Fe 25Cr



**B** Co15Cr 8Al

Figure 8.



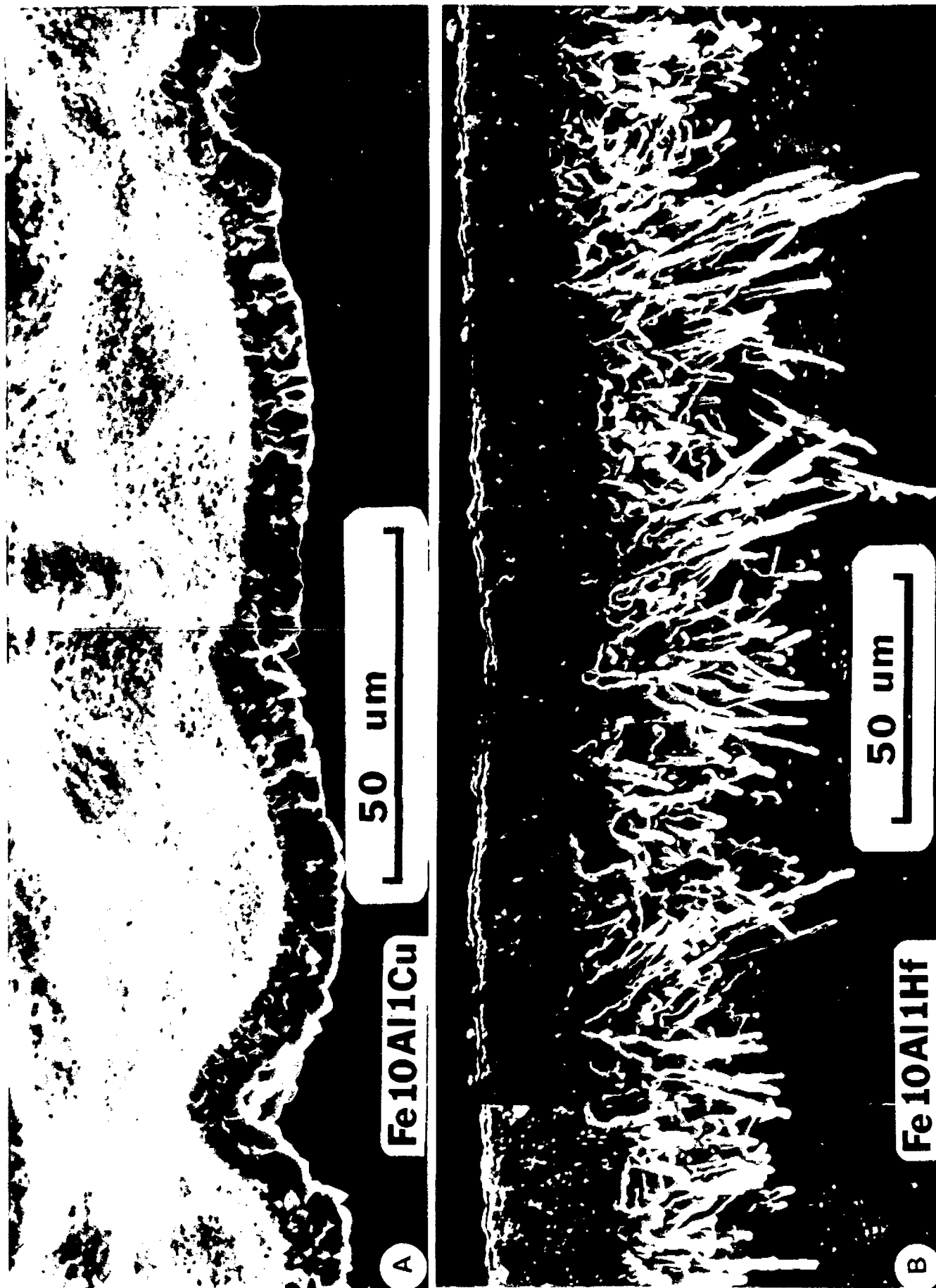


Figure 9.

XBB 828-7488

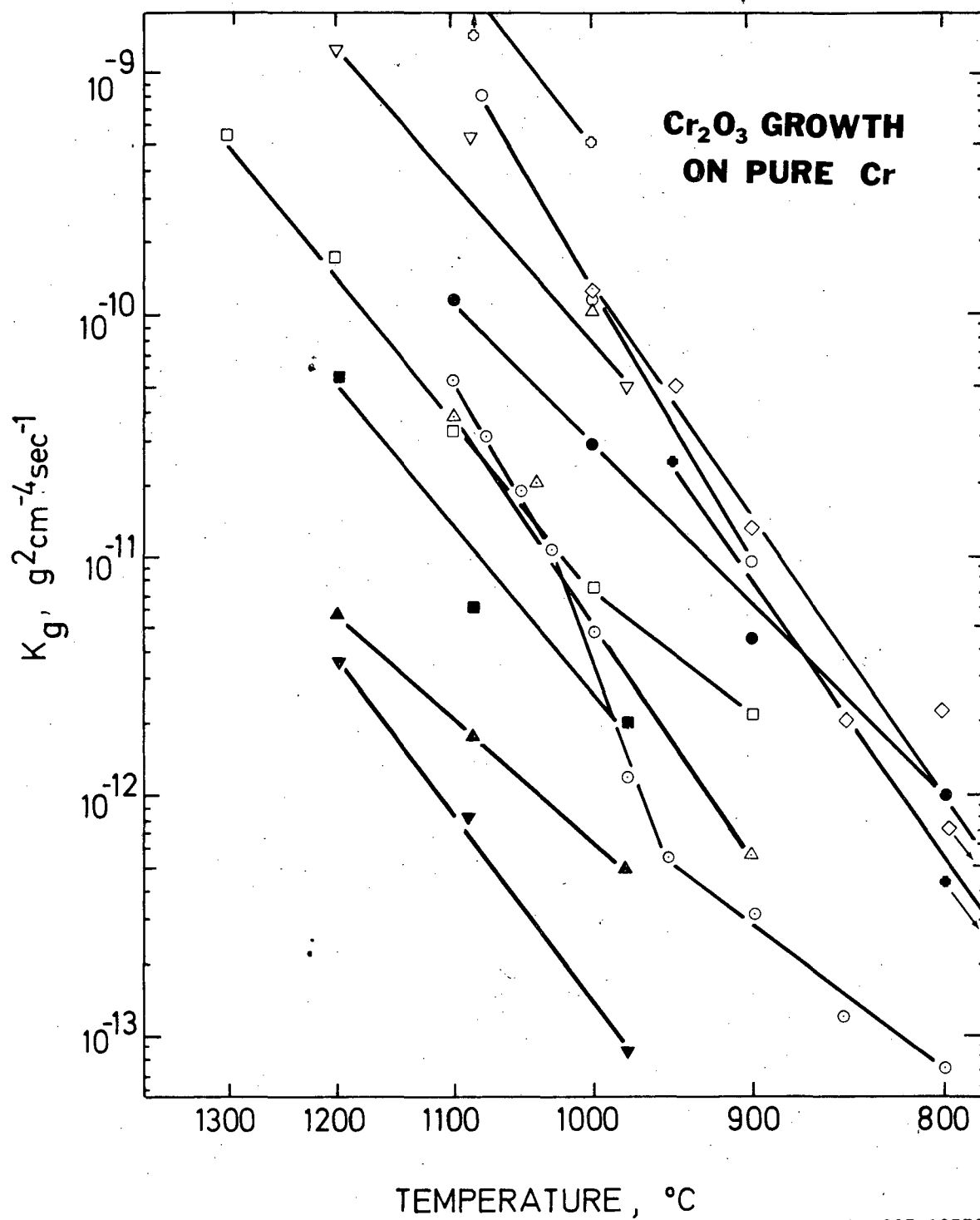


Figure 10.

XBL 827-10772

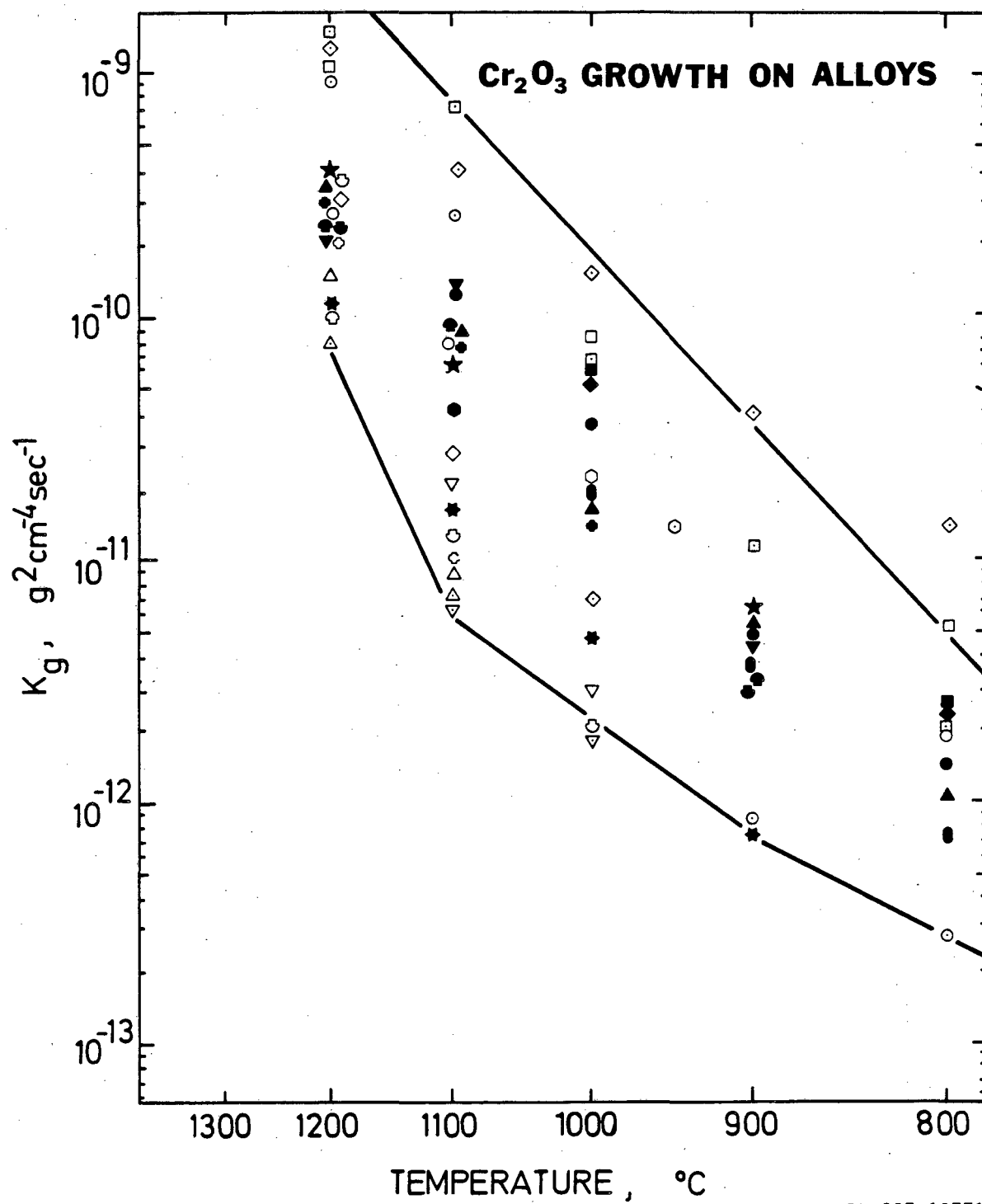


Figure 11.

XBL 827-10771

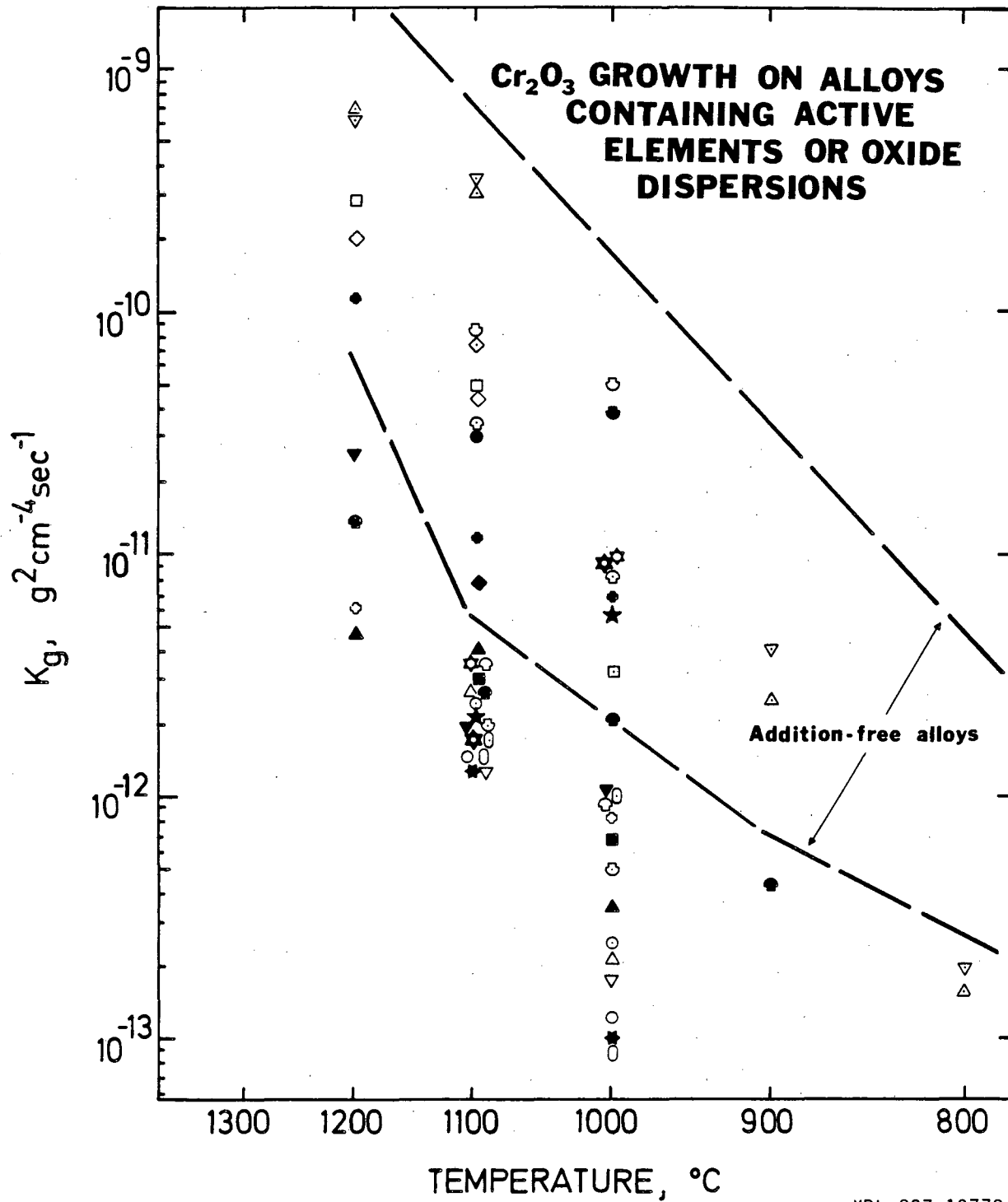
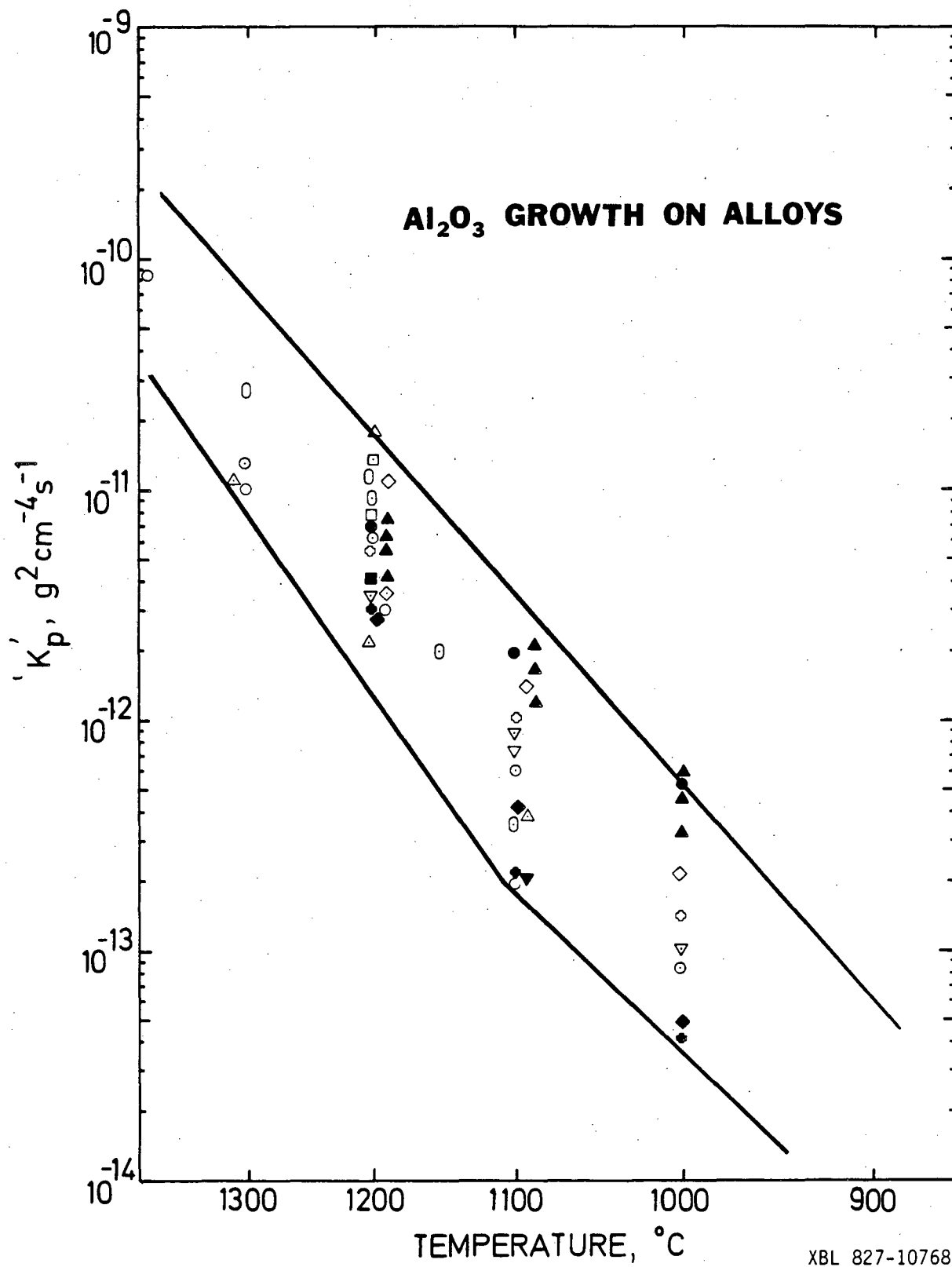


Figure 12.

XBL 827-10770



XBL 827-10768

Figure 13.

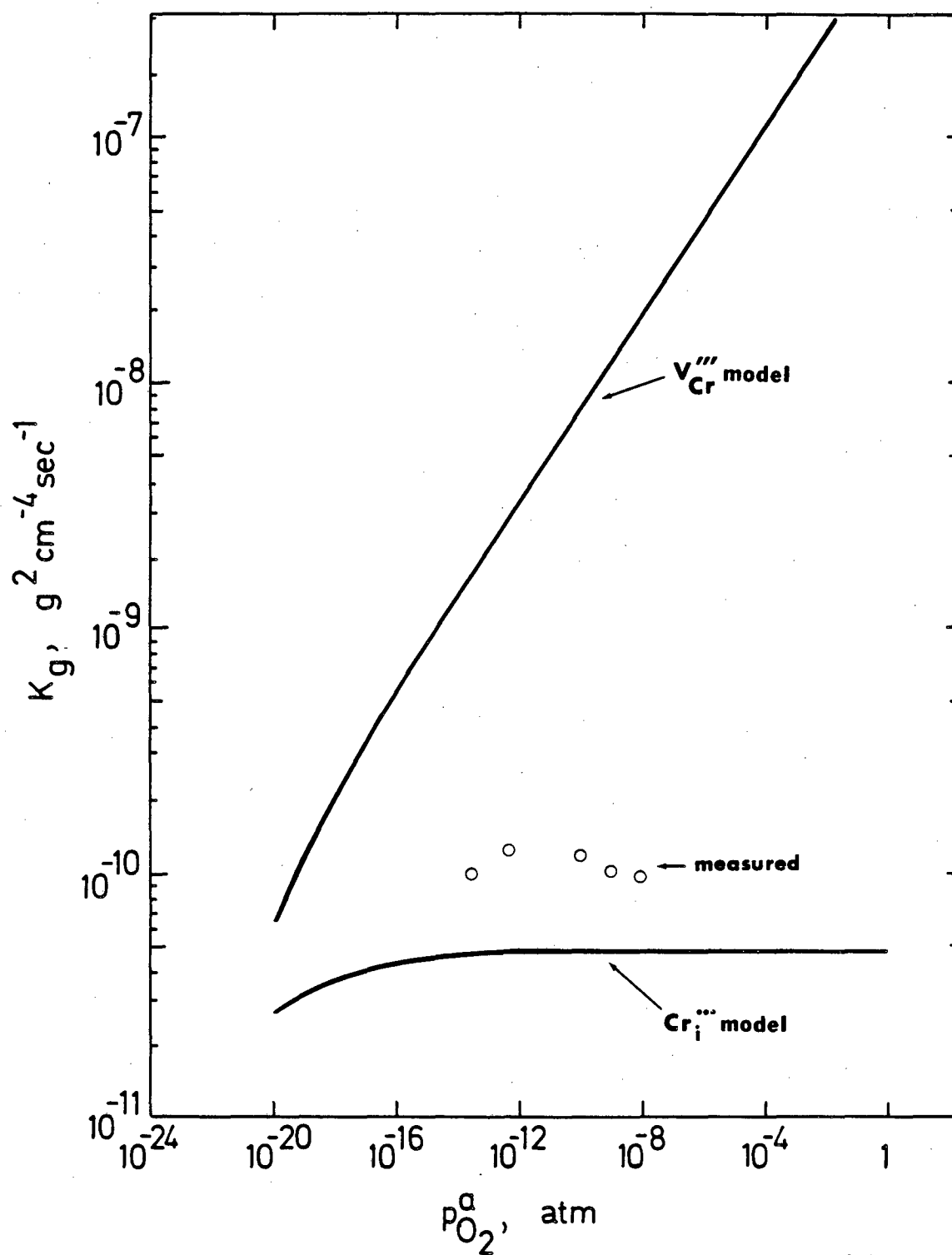
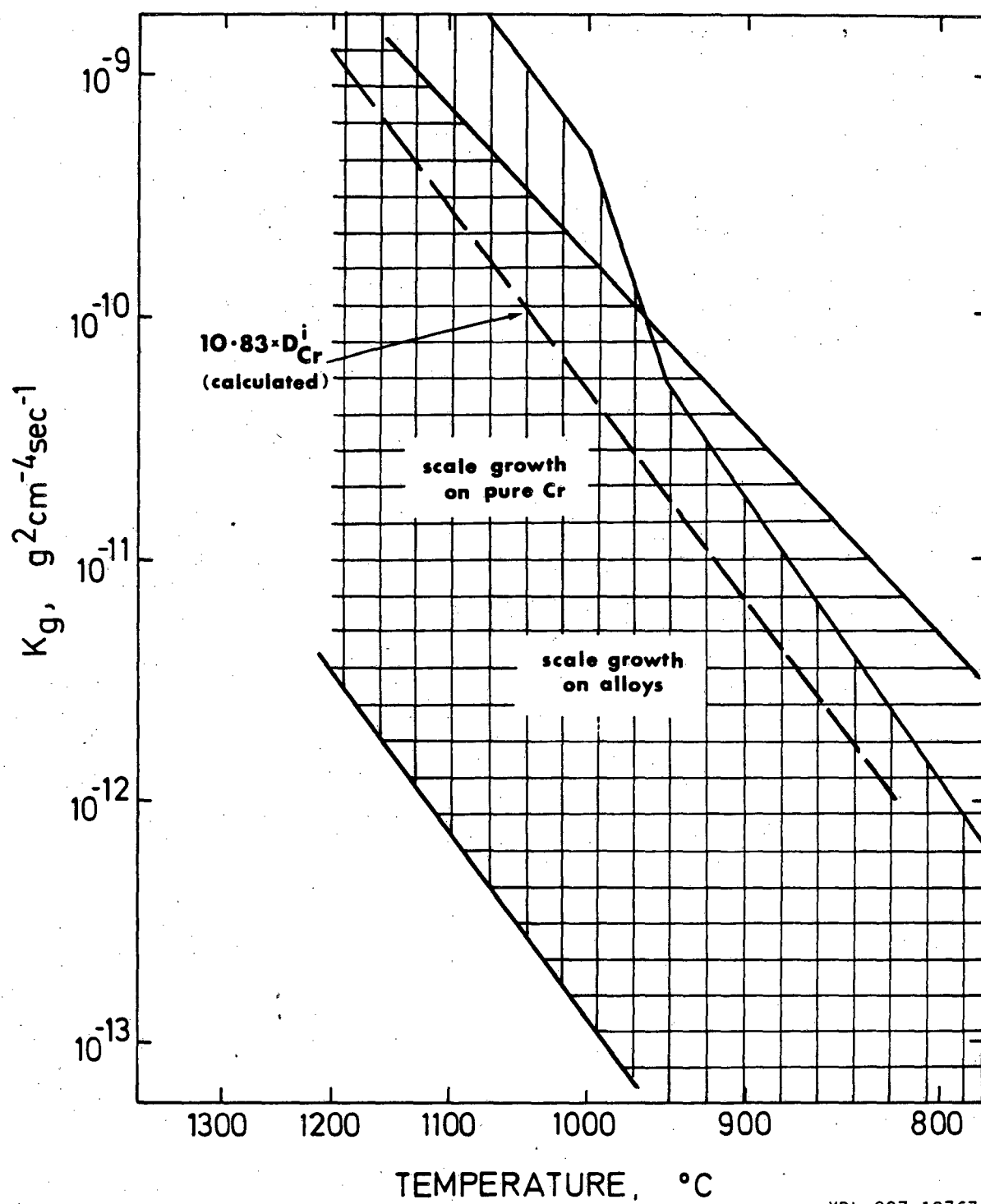


Figure 14.

XBL 827-10769



XBL 827-10767

Figure 15.

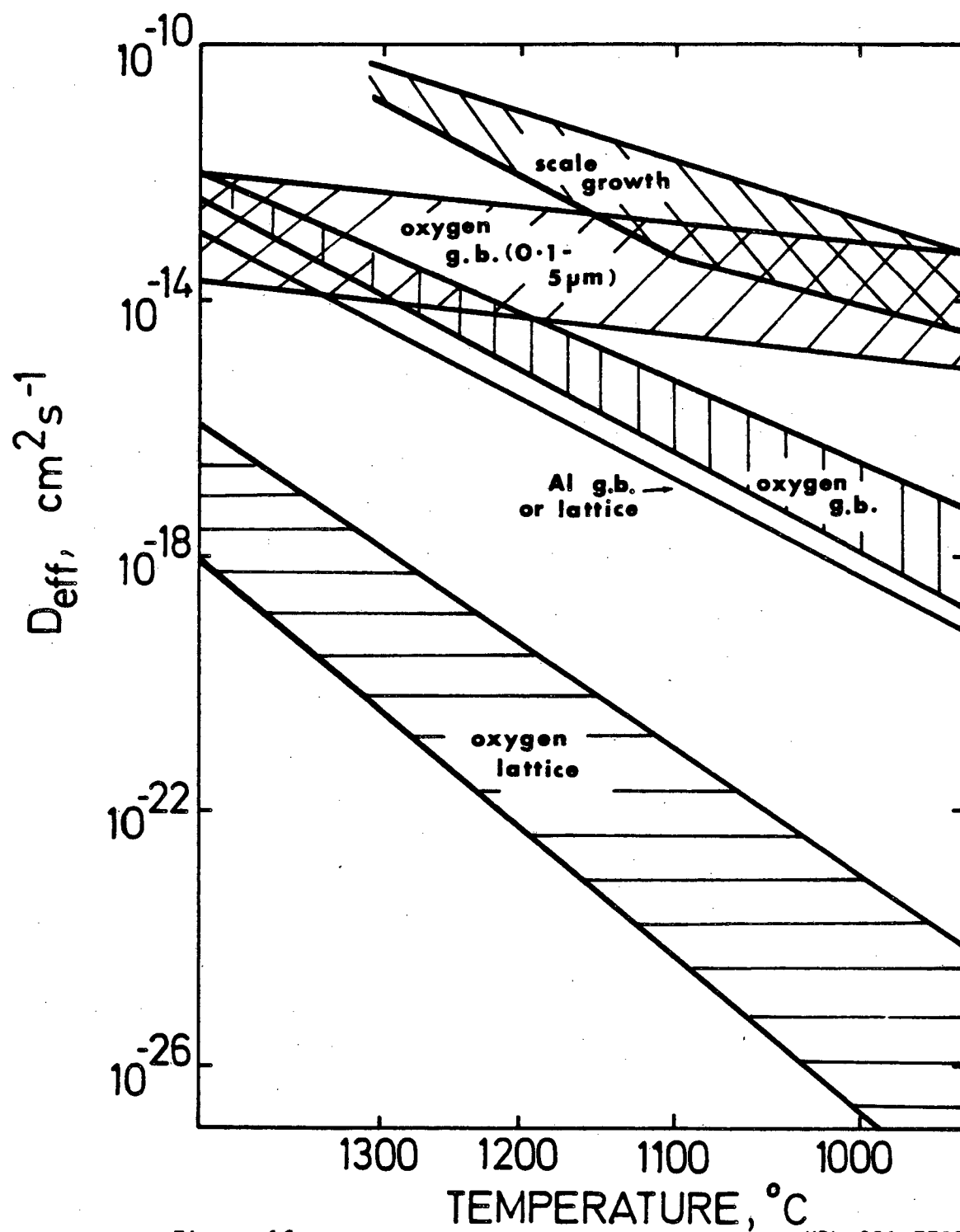


Figure 16.

XBL 821-7727



This report was done with support from the Department of Energy. Any conclusions or opinions expressed in this report represent solely those of the author(s) and not necessarily those of The Regents of the University of California, the Lawrence Berkeley Laboratory or the Department of Energy.

Reference to a company or product name does not imply approval or recommendation of the product by the University of California or the U.S. Department of Energy to the exclusion of others that may be suitable.

TECHNICAL INFORMATION DEPARTMENT  
LAWRENCE BERKELEY LABORATORY  
UNIVERSITY OF CALIFORNIA  
BERKELEY, CALIFORNIA 94720